J. Fluid Mech. (2013), *vol.* 721, *pp.* 484–513.
doi:10.1017/jfm.2013.67

Flame wrinkle destruction processes in harmonically forced, turbulent premixed flames

Dong-Hyuk Shin and Timothy Lieuwen†

School of Aerospace Engineering, Georgia Institute of Technology, Atlanta, GA 30332, USA

(Received 18 September 2012; revised 3 December 2012; accepted 24 January 2013;
first published online 19 March 2013)

This paper describes analyses of the nonlinear dynamics of harmonically forced, turbulent premixed flames. A key objective of this work is to analyse the ensemble-averaged dynamics of the flame front position, $\langle\xi\rangle$, excited by harmonic forcing of amplitude ε, in the presence of stochastic flow fluctuations of amplitude μ. Low-amplitude and/or near-field effects are quantified by a third-order perturbation analysis, while the more general case is analysed computationally by solving the three-dimensional level-set equation, extracting the instantaneous flame position, and ensemble averaging the results. We show that different mechanisms contribute to smoothing of flame wrinkles, manifested as progressive decay in the magnitude of $\langle\xi\rangle$. Near the flame holder, random phase jitter, associated with stochastic velocity fluctuations tangential to the flame, is dominant. Farther downstream, propagation of the ensemble-averaged front normal to itself at the time-averaged turbulent burning velocity, $\overline{S_{T,eff}}$, leads to destruction of wrinkles, analogous to the laminar case, an effect that scales with μ. A second, new result is the demonstration that the ensemble-averaged turbulent burning velocity, $S_{T,eff}(s,t)$, is modulated by the harmonic forcing, i.e. $S_{T,eff}(s,t) = \overline{S_{T,eff}(s)} + S'_{T,eff}(s,t)$, where $S'_{T,eff}$ has an inverse dependence upon the instantaneous, ensemble averaged-flame curvature, an effect that scales with ε and μ. We show that this curvature dependence follows from basic application of Huygens propagation to flames with stochastic wrinkling superimposed upon base curvature. This effect also leads to smoothing of flame wrinkles and is analogous to stretch processes in positive-Markstein-length, laminar flames.

Key words: combustion, reacting flows, turbulent reacting flows

1. Introduction

This paper describes the spatio-temporal characteristics of harmonically forced turbulent, premixed flames, in order to understand the influence of stochastic flow fluctuations upon the ensemble-averaged dynamics of the front. Its focus upon harmonic oscillations is motivated by the problem of combustion instabilities (Lieuwen & Yang 2005), which have emerged as one of the most important operability issues associated with low-emissions combustion technology. While approaches for analysing the combustor system dynamics have been developed (Dowling 1999), more understanding is required on the physical processes controlling the response of turbulent flames to harmonic flow perturbations (Huang & Yang 2009). This

† Email address for correspondence: tim.lieuwen@aerospace.gatech.edu

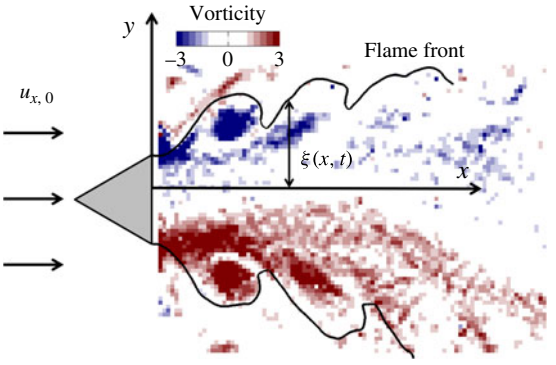

FIGURE 1. (Colour online) Instantaneous image of the flame front location and vorticity field. Reproduced from Shanbhogue (2008).

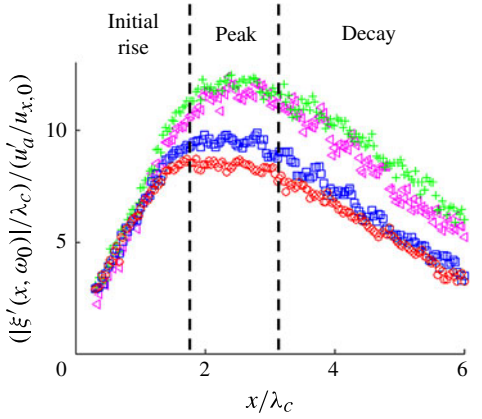

FIGURE 2. (Colour online) Measured dependence of flame front fluctuation magnitude for a circular bluff body with 12.7 mm diameter. ∘, $u'_a = 0.033$ m s^{-1}; □, $u'_a = 0.026$ m s^{-1}; +, $u'_a = 0.018$ m s^{-1}; ◁, $u'_a = 0.015$ m s^{-1}. Conditions: $\omega_0/2\pi = f_0 = 180$ Hz, $u_{x,0} = 2.27$ m s^{-1} and $\lambda_c = u_{x,0}/f_0$ (Shanbhogue 2008).

understanding is needed to develop rational approaches to prevent the occurrence of undesirable combustion instability, either in the design phase or through active control (McManus, Poinsot & Candel 1993). This paper closely follows a recent study analysing the relative roles of flame stretch and kinematic restoration processes in harmonically forced, laminar flames (Shin & Lieuwen 2012).

The key objective of the present study is to consider the effect of broadband turbulent forcing on the ensemble-averaged flame response at the excitation frequency. We briefly summarize the key flame features motivating this study next, summarizing the presentation from Shin & Lieuwen (2012), and then discuss the effects of simultaneous discrete frequency and stochastic flow excitation.

Figure 1 illustrates a typical image of the instantaneous edge of a flame forced by axial acoustic oscillations at a frequency, ω_0. These acoustic fluctuations excite vortical disturbances whose influence on the flame is evident from the periodic wrinkling on the flame, quantified with the variable $\xi(x, t)$.

Figure 2 shows the Fourier transform of $\xi(x, t)$ at the forcing frequency, $\omega = \omega_0$ (denoted as $|\xi(x, \omega_0)|$), for different upstream acoustic velocity amplitudes, u'_a. The

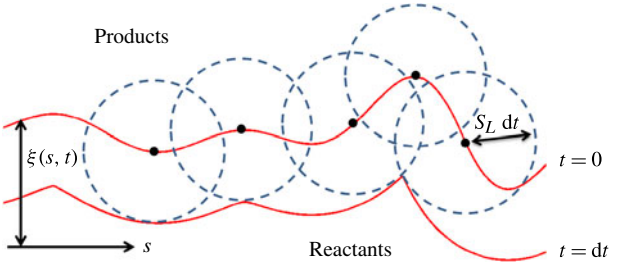

FIGURE 3. (Colour online) Instantaneous snapshots of an initially wrinkled flame front propagating into a quiescent flow with a constant burning velocity.

plot labels several generic features of the flame response, $|\xi(x,\omega_0)|$. First, $|\xi(x,\omega_0)|$ starts near zero and grows monotonically with downstream distance. This near-flame-holder behaviour is controlled by flame anchoring, and its growth rate is proportional to the velocity component normal to the time-averaged flame (Shanbhogue *et al.* 2009*a*). Next, after this initial wrinkle amplitude growth region, the flame response exhibits a peak, or even multiple local maxima. The data shown in figure 2 show a single peak. This peak is due to interference effects that occur due to the difference in propagation velocity in vortical flow disturbances exciting the flame, and the velocity with which these excited wrinkles propagate along the flame front.

Downstream of this peak, the flame wrinkle amplitude decays either monotonically or in an oscillatory fashion. It is this 'far-field' decay process which is the key focus of this study. Prior studies have demonstrated quantitative success in predicting the flame wrinkle gain and phase behaviour in the growth and peaking region (Shin *et al.* 2011). However, the decay region is much more complex because, as discussed next, it is intrinsically nonlinear and influenced by nonlinear coupling between narrowband and stochastic processes. Indeed, the nonlinear effects, which are negligible or weak in the initial 'rise' and 'peak' region of the flame response envelope, dominate the far-field decay region.

This decay region is influenced by both wrinkle excitation and destruction processes (Shanbhogue *et al.* 2009*a*). First, the decay rate in the excitation velocity source disturbing the flame is important; i.e. if the disturbance velocity persists indefinitely downstream, flame wrinkles are excited continually. This disturbance decay process is often associated with the dissipation rate of vortical disturbances in the shear layers. Second, the flame wrinkles themselves are dissipated by flame propagation mechanisms, which lead to a decrease in $|\xi(x,\omega_0)|$ once the excitation source has been removed. Flame wrinkles are smoothed out by two effects: kinematic restoration and stretch processes in thermo-diffusively stable flames (Law & Sung 2000; Shin & Lieuwen 2012).

We next summarize the characteristics of these two processes in laminar, iso-density flames, summarizing numerical and theoretical results from Shin & Lieuwen (2012). Kinematic restoration leads to an amplitude-dependent (i.e. nonlinear) smoothing of flame wrinkles. The reason for this smoothing is illustrated in figure 3, which shows an initially wrinkled flame that is propagating in a quiescent flow. These instantaneous snapshots illustrate that the leading parts of the flame propagate outward and consume the trailing-edge portions of the flame. This leads to a progressive change in wrinkle scale size and a monotonic decrease in wrinkle height.

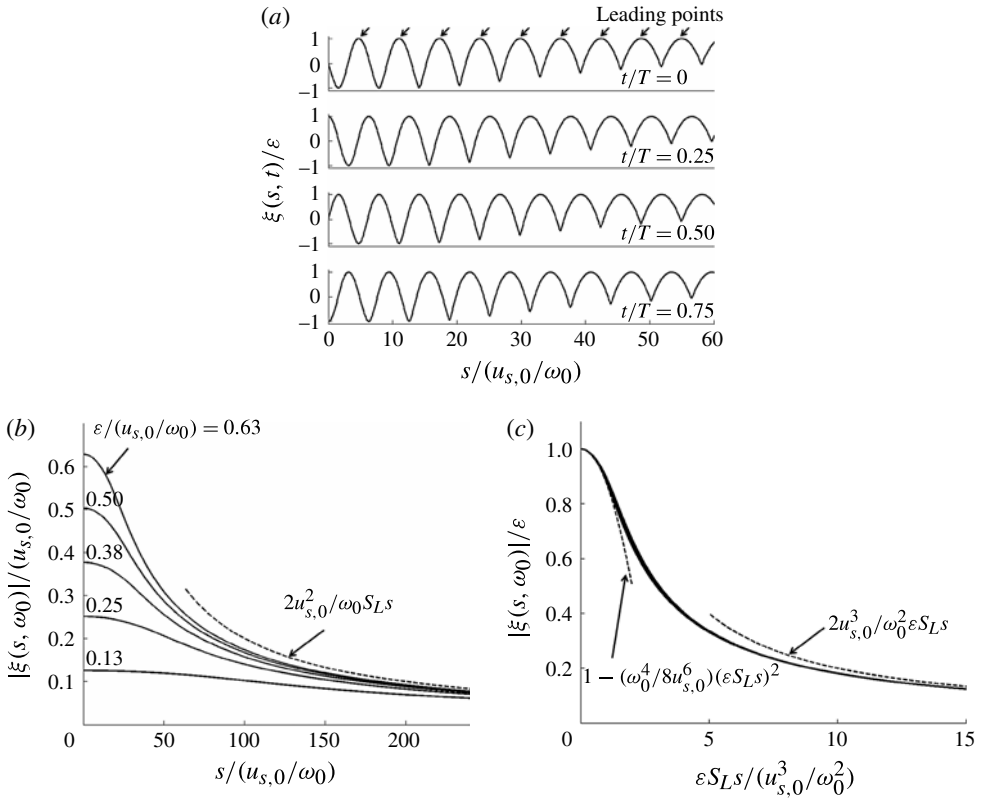

FIGURE 4. (*a*) Instantaneous computed flame front position, ξ, at four instances during a forcing period, T. (*b*) Dependence of laminar flame position magnitude on downstream distance at different excitation amplitudes. (*c*) Dependence of scaled flame position magnitude on scaled downstream distance for the same excitation amplitudes as in (*b*). Dashed lines denote asymptotic solutions for near and far fields, respectively (Shin & Lieuwen 2012).

This process can be understood from the following exact solution of the level-set equation in an iso-density flow using the Hopf–Lax formula (Evans 1997), where a wrinkled flame front, ξ_{init}, propagates in a quiescent flow (the governing equation which this solution is derived from is presented in (2.2)) as a function of the transverse coordinate, s and time, t, as:

$$\xi(s,t) = \min_{s-S_L t<s^*<s+S_L t} (\xi_{init}(s^*) - \sqrt{(S_L t)^2 - (s-s^*)^2}), \tag{1.1}$$

where S_L the laminar burning velocity and s^* is a variable ranging between the indicated values. This solution describes Huygens propagation (Huygens 1962), where the flame position is defined by the leading edge of a series of arcs originating from the initial flame front. To illustrate, the evolution in flame positions from time $t = 0$ to $t = \mathrm{d}t$ is drawn in figure 3 that shows this flame area destruction.

To illustrate this kinematic restoration effect in an anchored flame with tangential flow, $u_{s,0}$, figure 4(*a*) plots computations of the spatial dependence of $\xi(s,t)$ for a

flame that is anchored to an oscillatory flame holder, where $\xi(s=0,t)=\varepsilon\ \sin(\omega_0 t)$, emulating the experiments from Petersen & Emmons (1961).

Figure 4(*a*) shows the harmonic excitation in flame position near the flame holder and the axial convection of these wrinkles. Farther downstream, the propagation of the front normal to itself becomes increasingly evident, manifested in the cusping of the trailing edge of the front due to merging of the two flame branches. Note how the height of the flame wrinkle decreases with downstream distance.

One measure for quantifying the rate of decrease in wrinkle size is the dependence of the flame wrinkle amplitude at the forcing frequency, $|\xi(s,\omega_0)|$ upon downstream distance, s, where $|\xi(s,\omega)|$ denotes the gain of Fourier transform of $\xi(s,t)$. Calculations showing this dependence are plotted in figure 4(*b*) for five disturbance amplitudes, and in a scaled fashion in figure 4(*c*).

Figure 4(*b*) clearly shows the decay in magnitude of the flame wrinkle with downstream distance. Note also how $|\xi(s,\omega_0)|$ exhibits two different behaviours near and far from the attachment point. Near the flame holder, the decay rate in $|\xi(s,\omega_0)|$ increases nonlinearly with forcing amplitude, ε; e.g. the flame wrinkle amplitude with $\varepsilon=0.63(u_{s,0}/\omega_0)$ decays much faster than that with $\varepsilon=0.13(u_{s,0}/\omega_0)$. Farther downstream, however, note how all the results converge to a common curve, independent of forcing amplitude. In this region, the flame response, $|\xi(s,\omega_0)|/\varepsilon$, decays inversely with $\varepsilon S_L s$ as shown in figure 4(*c*), where the same data are plotted with scaled parameters. Here, the flame wrinkle is controlled by the leading points that are indicated in figure 4(*a*), and the decay rate is independent of initial excitation amplitude. These two asymptotic tendencies are given by Shin & Lieuwen (2012):

$$\frac{|\xi(s,\omega_0)|}{\varepsilon}=\begin{cases}1-\dfrac{\omega_0^4}{8u_{s,0}^6}\ (\varepsilon S_L s)^2 & \text{for } s\ll 1,\\ \dfrac{2u_{s,0}^3}{\omega_0^2}\ \dfrac{1}{\varepsilon S_L s} & \text{for } s\gg 1.\end{cases}\tag{1.2}$$

Consider next the second process responsible for smoothing of flame wrinkles: flame stretch. Flame wrinkles are also smoothed by stretch processes in thermo-diffusively stable flames, an effect which can be understood from linear analysis (Wang, Law & Lieuwen 2009). As shown in Shin & Lieuwen (2012), the linearized, weak stretch solution for the flame wrinkle behaviour for the oscillatory flame holder problem considered above is given by:

$$\frac{|\xi(s,\omega_0)|}{\varepsilon}=\exp\left(-\frac{\omega_0^2}{u_{s,0}^3}\,\sigma S_L s\right),\tag{1.3}$$

where σ is the Markstein length. Although this paper will focus on stretch-insensitive flames, we will show that one of the impacts of stochastic fluctuations on the ensemble-average flame dynamics is analogous to a stretch effect and will return to this equation later.

With this as background, we next consider stretch-free flame dynamics in flows with both harmonic and turbulent flow components. These disturbances nonlinearly interact and introduce new effects (Creta & Matalon 2011). For example, both deterministic and stochastic processes contribute to smoothing of the ensemble-averaged harmonic flame wrinkle (Lieuwen 2003; Hemchandra, Peters & Lieuwen 2011). We will show in this paper that this occurs through both stochastic kinematic restoration and phase jitter effects which do not average to zero.

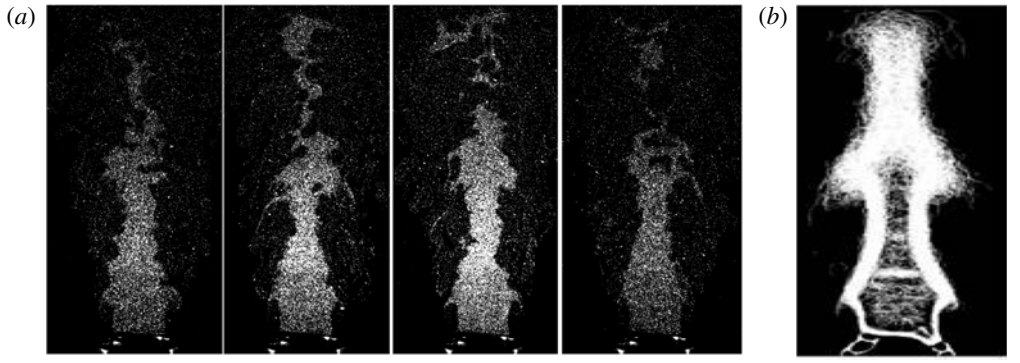

FIGURE 5. (*a*) Four instantaneous phase-locked Mie scattering images from a turbulent propane Bunsen flame excited by a longitudinal acoustic disturbance. (*b*) Overlay of instantaneous flame edges showing flame brush and coherent wrinkling on the flame induced by the harmonic forcing (Thumuluru 2010).

To illustrate the problem of interest, figure 5 shows experimental Mie scattering images of a harmonically excited, turbulent Bunsen flame, illustrating the simultaneous presence of the coherent and broadband wrinkling on the flame front. The four instantaneous images in figure 5(*a*) show significant turbulent wrinkling of the flame front. Figure 5(*b*) overlays a number of flame edges extracted from these instantaneous images at the same phase, clearly showing the coherent wrinkling on the flame induced by the harmonic forcing. This coupling between harmonic and stochastic processes on turbulent flames is not well understood (Lee & Santavicca 2003; Ayache *et al.* 2010; Kim & Hochgreb 2011). The specific objective of this work is to analyse this problem and determine the interactions and relative significance of the deterministic and stochastic components of this problem in controlling the dynamics of harmonically excited flame wrinkles, such as their decay rate.

2. Formulation

In this section we consider a harmonically oscillating flame holder, emulating the experimental study of Petersen & Emmons (1961) shown in figure 6, in the presence of a stochastically oscillatory background flow. This is a useful problem for this study as the amplitude of flame wrinkling, within an iso-density, stretch-free and linear analysis framework, is constant and independent of axial location; i.e. $|\xi(x, \omega_0)| = |\xi(x = 0, \omega_0)|$. In contrast, the harmonic-velocity-forced flame has a spatially modulated flame wrinkling character, as shown in figure 2, leading to a complex modulation of nonlinear processes (Huang *et al.* 2009; Karimi *et al.* 2009; Hemchandra *et al.* 2011). This oscillating flame holder problem allows us to develop relatively simple expressions for the key dimensionless parameters controlling the problem, and thus, to isolate the critical processes controlling the far-field evolution of harmonically forced flames.

The investigated geometry is shown in figure 7. The coordinate system is aligned with the unperturbed flame position, so that the s and n coordinates are tangential and normal to the unperturbed flame respectively, with the z coordinate pointing in the third orthogonal direction out of the page. The flow field is prescribed and the

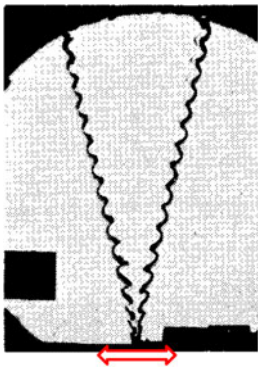

FIGURE 6. (Colour online) Visualization of a propane flame stabilized on a transversely oscillating flame holder at 625 Hz ($\phi = 1$, $u_{x,0} = 4.8$ m s^{-1}) (Petersen & Emmons 1961).

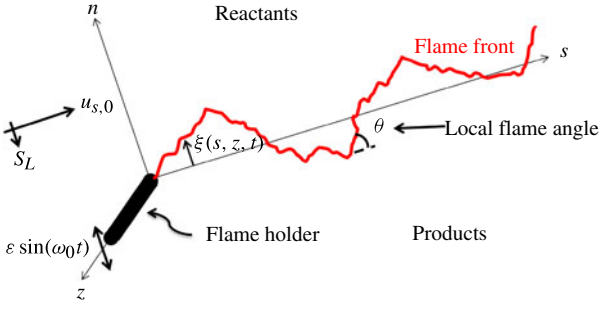

FIGURE 7. (Colour online) Diagram of flame/flow configuration and the coordinates (ξ: flame front location).

flame holder vibrates in the n-direction, creating wrinkles on the flame at $s = 0$ which propagate downstream.

The principal assumptions regarding the flame dynamics made in this analysis are that: (i) the flame is a thin, two-dimensional interface, dividing reactants and products; (ii) there is a negligible density jump across the flame; (iii) the flame speed, S_L, is constant; and (iv) the flame remains attached to the flame holder. Following assumption (i), the instantaneous location of the flame front is determined from the G-equation (Williams 1985), given by:

$$\frac{\partial G}{\partial t} + u_s \frac{\partial G}{\partial s} + u_n \frac{\partial G}{\partial n} + u_z \frac{\partial G}{\partial z} = S_L \left[\left(\frac{\partial G}{\partial s} \right)^2 + \left(\frac{\partial G}{\partial n} \right)^2 + \left(\frac{\partial G}{\partial z} \right)^2 \right]^{1/2}. \quad (2.1)$$

The key effect of assumption (ii) is that the stochastic velocity fluctuations (u_s, u_n, u_z) are prescribed – an oscillatory flame sheet with a finite density change otherwise influences the approach flow. As this is an important assumption, we next discuss how the results are influenced by it. This issue has been discussed by a number of workers (Kuramoto & Tsuzuki 1976; Sivashinsky 1977; Matalon & Matkowsky 1982; Lee & Lieuwen 2003; Creta, Fogla & Matalon 2011). In general, flames have finite density jumps, although the weak density jump across flames is an important limit in its own right, as many practical applications utilizing highly

compressed (and therefore preheated, such as modern aircraft engines), vitiated (such as in afterburners), or flows with significant regenerative heat transfer (Tsuji *et al.* 2002; Dally, Riesmeier & Peters 2004) have small density jumps. An important qualitative effect introduced by the density jump is the Darrieus–Landau flame instability, where the approach flow field is altered in such a way as to cause amplification of flame wrinkles (Matalon & Matkowsky 1982). The character of this hydrodynamic instability is altered by harmonic forcing as well. For example, low-amplitude harmonic excitation leads to stabilization of the hydrodynamic instability, while large-amplitude forcing introduces a new parametric instability, resulting in oscillation of the flame sheet at the subharmonic of the forcing frequency (Searby & Rochwerger 1991). In addition, Creta & Matalon (2011) have analysed the interactions of broadband flow fluctuations and a hydrodynamically unstable flame, showing the augmentation of the turbulent flame brush thickness and the turbulent flame speed by flame instability.

The key focus of this paper is the effect of nonlinear interactions between harmonic and broadband flow disturbances on the ensemble-averaged flame dynamics. As such, while these additional physics can be included in computations (e.g. see Rastigejev & Matalon 2006; Moureau, Fiorina & Pitsch 2009), analytical results such as presented in this paper are extremely challenging due to the coupling of the flame and flow at the moving flame boundary. We have tried to focus on a problem that brings out these points with maximum clarity, and thus consider the iso-density limit. However, an important follow-on to this work should be to include these effects and the additional physics they introduce.

Returning to the assumptions, we next consider assumption (iii) and its implications on the results. In general, flames are stretch sensitive, implying that flame curvature and flow strain cause modification of the burning velocity in space and time (Matalon 1983). This is a stabilizing and destabilizing influence in positive- and negative-Markstein-length flames, respectively. Thus, as shown by Wang *et al.* (2009) and discussed in the previous section, flame stretch processes in thermo-diffusively stable flames lead to smoothing of flame wrinkles. In contrast, turbulent flow fluctuation influences on flame wrinkling can be amplified in thermo-diffusively unstable flames. Again, it is appropriate to consider the zero stretch sensitive case as a starting point for this analysis because this is a good descriptor of flames with small Markstein lengths, as well as enabling development of a problem whose results can be analysed with maximum clarity.

For small velocity fluctuations, the flame front position is single-valued, an approximation that breaks down at high-amplitude fluctuations. We will utilize this assumption for the analytical calculations presented in this paper, but not for the computations. For a single-valued flame position, a substitution, $G = n - \xi(s, z, t)$, leads to the following equation for the flame position, $\xi(s, z, t)$:

$$\frac{\partial \xi}{\partial t} + u_s \frac{\partial \xi}{\partial s} - u_n + u_z \frac{\partial \xi}{\partial z} = S_L \left[1 + \left(\frac{\partial \xi}{\partial s} \right)^2 + \left(\frac{\partial \xi}{\partial z} \right)^2 \right]^{1/2}. \tag{2.2}$$

The velocity field shown in figure 7 is written in terms of mean and perturbation quantities as:

$$u_s = u_{s,0} + \mu f_s(s, n, z, t)|_{n=\xi}, \tag{2.3a}$$

$$u_n = -S_L + \mu f_n(s, n, z, t)|_{n=\xi}, \tag{2.3b}$$

$$u_z = \mu f_z(s, n, z, t)|_{n=\xi}, \tag{2.3c}$$

where μ and f_i denote the magnitude of the velocity fluctuation and the shape function, respectively. The turbulence intensity is $\sqrt{3}\mu$ with $\langle f_i^2 \rangle = 1$.

With the velocity expressions (2.3), the single-valued flame dynamics equation (2.2) is rewritten as:

$$\frac{\partial \xi}{\partial t} + u_{s,0}\frac{\partial \xi}{\partial s} = \underbrace{S_L\left\{\left[1+\left(\frac{\partial \xi}{\partial s}\right)^2+\left(\frac{\partial \xi}{\partial z}\right)^2\right]^{1/2}-1\right\}}_{\text{Kinematic restoration}} + \underbrace{\mu\left[-f_s\frac{\partial \xi}{\partial s}+f_n-f_z\frac{\partial \xi}{\partial z}\right]}_{\text{Turbulent flow forcing}}. \tag{2.4}$$

Here, the first and the second terms on the right-hand side describe changes to the convecting flame wrinkle, $\xi(t - s/u_{s,0})$, through kinematic restoration and turbulent flow forcing, respectively. Because of nonlinearities associated with convection (e.g. $f_s\partial\xi/\partial s$) and kinematic restoration (e.g. $[1 + (\partial\xi/\partial s)^2 + (\partial\xi/\partial z)^2]^{1/2}$), these two terms interact.

Two boundary conditions are needed. First, it is assumed that the flame is attached to the flame holder which oscillates in the n-direction as:

$$\xi(s = 0, z, t) = \varepsilon\ \sin(\omega_0 t), \tag{2.5}$$

where ε and ω_0 denote the magnitude and angular frequency of the flame holder oscillation, respectively. Second, a non-reflecting boundary condition is applied at the downstream end of the calculation domain, so that information only propagates along the flame in the flow direction.

The stochastic flow fluctuations in (2.3) are assumed to be: (i) isotropic; (ii) incompressible; (iii) Gaussian distributed; (iv) propagating with the flow as per Taylor's hypothesis; and (v) have Eulerian space/time correlations that decay exponentially over a longitudinal length scale, L_{11}, as (Hinze 1975):

$$\langle f_s(s, n, z, t) f_s(s + r, n, z, t)\rangle = \exp\left(-\frac{\pi}{4}\left(\frac{r}{L_{11}}\right)^2\right). \tag{2.6}$$

Taylor's hypothesis with the specified velocities in (2.3) implies:

$$f_i(s, n, z, t + \Delta t) = f_i(s - u_{s,0}\Delta t, n + S_L\Delta t, z, t) \quad \text{for } i = s, n, z. \tag{2.7}$$

Based on (2.6) and (2.7), all two-point correlations can be derived from isotropy relations (Pope 2000) as listed in appendix A. For Gaussian random variables, all higher-order correlations can be derived from sum and products of two-point correlations and all odd-order correlations are zero (Frenkiel & Klebanoff 1967; Bendat & Piersol 2011). Similar procedures have been used in other studies of this nature (Aldredge & Williams 1991; Creta *et al.* 2011). These stochastic fluctuations will be referred to in this paper as 'turbulent flow fluctuations', but it should be kept in mind that they actually describe random flow fluctuations that emulate certain, but not all, features of Navier–Stokes turbulence. For example, assumptions (i)–(v) above are common features of Navier–Stokes turbulence, but the stochastic fluctuations do not emulate other features, such as the phase characteristics between different frequency/wavenumber spectral components. Lastly, the following

non-dimensionalization scheme is used for simplification:

$$\tilde{s} = s/(u_{s,0}/\omega_0), \qquad \tilde{z} = z/(u_{s,0}/\omega_0), \qquad \tilde{n} = n/(u_{s,0}/\omega_0), \tag{2.8a}$$

$$\tilde{\xi} = \xi/(u_{s,0}/\omega_0), \quad \tilde{L}_{11} = L_{11}/(u_{s,0}/\omega_0), \quad \tilde{\varepsilon} = \varepsilon/(u_{s,0}/\omega_0), \tag{2.8b}$$

$$\tilde{t} = \omega_0 t, \qquad \tilde{S}_L = S_L/u_{s,0}, \qquad \tilde{\mu} = \mu/u_{s,0}. \tag{2.8c}$$

The solutions to the full G-equation (2.1) are analysed computationally. Solutions of the single-valued ξ-equation (2.4) are analysed asymptotically. This asymptotic analysis is performed up to third-order in the oscillating amplitude, $\tilde{\varepsilon}$, and the turbulence intensity, $\tilde{\mu}$. The computational procedure is described next.

2.1. *Numerical simulation*

This section describes the computational approach used to solve the level-set equation (2.1). These computations closely follow previously reported work detailed in Sethian (1999) and Osher & Fedkiw (2003), and in Hemchandra & Lieuwen (2010) for this particular application. The level-set equation is solved using the semi-Lagrangian Courant–Isaacson–Rees scheme together with the back-and-forth error compensation and correction (BFECC) technique (Dupont & Liu 2007). This is a second-order scheme with low numerical dissipation and dispersion errors. The local level-set method is adopted to achieve significant reduction in computation time (Peng *et al.* 1999). The level-set field is reset to a signed distance function by solving an auxiliary re-distancing equation using the prescription of Dupont & Liu (2007).

The computational domain consists of $201 \times 201 \times 801$ grid cells with a spatial resolution of $(u_{s,0}/f_0)/100$, $L_{11}/10$, and a time step of $1/1000f_0$. Several grid convergence studies were performed. First, a grid study was performed for a laminar case with the baseline and factor-of-ten increased grid density, showing less than a 1 % difference in flame position at $\tilde{s} = 25$. A similar comparison of calculations using the baseline and factor-of-two increased density for the $\tilde{\mu} = 0.04$ case showed a 3 % difference in ensemble-averaged flame position at $\tilde{s} = 15$.

The instantaneous flame position is evaluated numerically from the level-set field using numerical approximations for the Heaviside function (Osher & Fedkiw 2003) and the delta function (Peter 2006). The numerical results are then phase-averaged over 160 ensembles to produce one time series in the forcing period.

In order to compare these computations with analytical results, it is necessary to calculate the ensemble-averaged flame positions, $\langle\tilde{\xi}\rangle$. At lower turbulence intensities, the instantaneous flame position is a single-valued function of $(\tilde{s}, \tilde{z})$ for the majority of time instants; e.g. the flame is multi-valued in less than 1 % of realizations for $\tilde{\mu} = 0.04$. However, the occurrence of multi-valuedness increases significantly with increasing turbulent intensity (see figure 8); e.g. in ∼25 % of the realizations for $\tilde{\mu} = 0.20$.

Different approaches can be used to specify the ensemble-averaged flame position in these cases. One approach is to turn each realization into a field of binarized values, with zero and unity denoting reactants and products, respectively. These fields can then be averaged and the ensemble-averaged value associated with some progress variable, $\widehat{C}$, such as $\langle\widehat{C}\rangle = 0.5$ (Driscoll 2008). This is a fairly standard way in which ensemble-averaged flame characteristics are presented in experimental turbulent combustion studies. The problem with this binarization approach, however, is that it is a nonlinear operation. Consequently, even for a single-valued flame front, the $\langle\widehat{C}\rangle = 0.5$ iso-contour describes the median (Shin 2012), not the mean, of the flame position. However, the asymptotic analysis quantifies the mean, so the

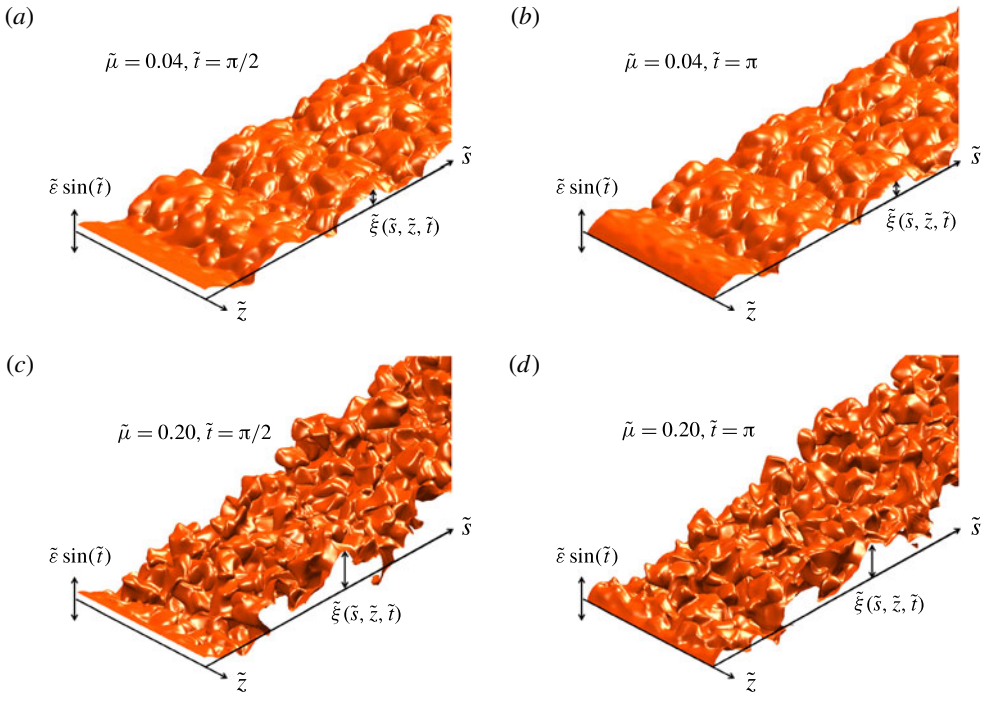

FIGURE 8. (Colour online) Instantaneous realizations of the flame sheet extracted from solution of the full level-set equation, (2.1) at $\tilde{t} = \pi/2$ and π. (*a*,*b*) $\tilde{\mu} = 0.04$, (*c*,*d*) $\tilde{\mu} = 0.20$ ($\tilde{S}_L = 0.25$, $\tilde{\varepsilon} = 0.65$, $\tilde{L}_{11} = 0.65$).

two calculation approaches cannot be quantitatively compared. Therefore, we did not utilize this progress variable approach. Rather, we extracted the instantaneous flame position coordinates and defined $\langle\tilde{\xi}\rangle$ as the average of each transverse value at a given axial location. This result leads to a consistent comparison approach for single-valued flames where the asymptotic analysis can be performed. Practically speaking, the difference between the two calculation approaches does not appear to be significant, as appendix B compares the $\langle\widehat{C}\rangle = 0.5$ iso-contour and $\langle\tilde{\xi}\rangle$ for a typical case showing that they are nearly identical.

2.2. *Asymptotic analysis*

Asymptotic analyses of the governing equations were performed to obtain insight into key parameters controlling the flame wrinkle decay rate. Since the objective of this analysis is to analyse nonlinear corrections to the flame response at the forcing frequency, the analysis must be obtained up to the third-order in $\tilde{\varepsilon}$ and $\tilde{\mu}$. The flame position, $\tilde{\xi}$, is expanded using the following two-parameter expansion in harmonic excitation amplitude, $\tilde{\varepsilon}$, and turbulence intensity, $\tilde{\mu}$, as:

$$\begin{aligned}\tilde{\xi}(\tilde{s},\tilde{z},\tilde{t}) = {} & \tilde{\varepsilon}\,\tilde{\xi}_{\varepsilon}(\tilde{s},\tilde{z},\tilde{t}) + \tilde{\mu}\,\tilde{\xi}_{\mu}(\tilde{s},\tilde{z},\tilde{t}) \\ & + \tilde{\varepsilon}^2\,\tilde{\xi}_{\varepsilon\varepsilon}(\tilde{s},\tilde{z},\tilde{t}) + \tilde{\varepsilon}\tilde{\mu}\,\tilde{\xi}_{\varepsilon\mu}(\tilde{s},\tilde{z},\tilde{t}) + \tilde{\mu}^2\,\tilde{\xi}_{\mu\mu}(\tilde{s},\tilde{z},\tilde{t}) \\ & + \tilde{\varepsilon}^3\,\tilde{\xi}_{\varepsilon\varepsilon\varepsilon}(\tilde{s},\tilde{z},\tilde{t}) + \tilde{\varepsilon}^2\tilde{\mu}\,\tilde{\xi}_{\varepsilon\varepsilon\mu}(\tilde{s},\tilde{z},\tilde{t}) + \tilde{\varepsilon}\tilde{\mu}^2\,\xi_{\varepsilon\mu\mu}(\tilde{s},\tilde{z},\tilde{t}) \\ & + \tilde{\mu}^3\,\tilde{\xi}_{\mu\mu\mu}(\tilde{s},\tilde{z},\tilde{t}) + O((\tilde{\varepsilon},\tilde{\mu})^4). \end{aligned} \tag{2.9}$$

The corresponding boundary conditions for each function are:

$$\tilde{\xi}_{\Theta}(\tilde{s}=0,\tilde{z},\tilde{t})=\begin{cases}\sin(\tilde{t}) & \text{if } \Theta=\varepsilon\\ 0 & \text{otherwise.}\end{cases} \tag{2.10}$$

After inserting the expansion (2.9) into (2.4) and matching terms with the same order, we obtain a series of partial differential equations for each function, $\tilde{\xi}_{\Theta}$. For example, the equation for $\tilde{\xi}_{\varepsilon\mu\mu}$ is:

$$\begin{aligned}\frac{\partial\tilde{\xi}_{\varepsilon\mu\mu}}{\partial\tilde{t}}+\frac{\partial\tilde{\xi}_{\varepsilon\mu\mu}}{\partial\tilde{s}}=\tilde{S}_L&\left(\frac{\partial\tilde{\xi}_{\mu}}{\partial\tilde{s}}\frac{\partial\tilde{\xi}_{\varepsilon\mu}}{\partial\tilde{s}}+\frac{\partial\tilde{\xi}_{\mu}}{\partial\tilde{z}}\frac{\partial\tilde{\xi}_{\varepsilon\mu}}{\partial\tilde{z}}+\frac{\partial\tilde{\xi}_{\varepsilon}}{\partial\tilde{s}}\frac{\partial\tilde{\xi}_{\mu\mu}}{\partial\tilde{s}}+\frac{\partial\tilde{\xi}_{\varepsilon}}{\partial\tilde{z}}\frac{\partial\tilde{\xi}_{\mu\mu}}{\partial\tilde{z}}\right)\\&-f_s\frac{\partial\tilde{\xi}_{\varepsilon\mu}}{\partial\tilde{s}}-\frac{\partial f_z}{\partial\tilde{n}}\frac{\partial\tilde{\xi}_{\varepsilon}}{\partial\tilde{z}}\tilde{\xi}_{\mu}-\frac{\partial f_z}{\partial\tilde{n}}\frac{\partial\tilde{\xi}_{\mu}}{\partial\tilde{z}}\tilde{\xi}_{\varepsilon}-\frac{\partial f_s}{\partial\tilde{n}}\frac{\partial\tilde{\xi}_{\varepsilon}}{\partial\tilde{s}}\tilde{\xi}_{\mu}\\&-\frac{\partial f_s}{\partial\tilde{n}}\frac{\partial\tilde{\xi}_{\mu}}{\partial\tilde{s}}\tilde{\xi}_{\varepsilon}-f_z\frac{\partial\tilde{\xi}_{\varepsilon\mu}}{\partial\tilde{z}}+\frac{\partial\tilde{f}_n}{\partial\tilde{n}}\tilde{\xi}_{\varepsilon\mu}+\frac{\partial^2\tilde{f}_n}{\partial\tilde{n}^2}\tilde{\xi}_{\varepsilon}\tilde{\xi}_{\mu}.\end{aligned} \tag{2.11}$$

Then, these equations are solved sequentially with the boundary condition (2.10). For example, the first-order solutions are:

$$\tilde{\xi}_{\varepsilon}=\sin(\tilde{t}-\tilde{s}), \tag{2.12a}$$

$$\langle\tilde{\xi}_{\mu}\rangle=0, \tag{2.12b}$$

where $\langle\ \rangle$ represents the ensemble average. Thus, the flame wrinkle amplitude is constant at the first-order; i.e. it does not decay in the absence of stretch or nonlinear effects, as discussed earlier. The solution, $\tilde{\xi}_{\varepsilon}$, mimics the forcing and convects downstream as a travelling wave at the tangential velocity, $u_{s,0}$.

The full solutions of these equations are quite lengthy and are presented in the lead author's thesis (Shin 2012). The particular focus of this study is the ensemble-averaged dynamics of $\tilde{\xi}$. Solutions for the ensemble-averaged flame position are:

$$\langle\tilde{\xi}_{\varepsilon\varepsilon}\rangle=\frac{1}{4}\tilde{S}_L\left[\tilde{s}+\tilde{s}\,\cos(2(\tilde{t}-\tilde{s}))\right], \tag{2.13}$$

$$\begin{aligned}\langle\tilde{\xi}_{\varepsilon\varepsilon\varepsilon}\rangle=&-\frac{1}{8}\tilde{S}_L^2\left[\tilde{s}^2\sin(\tilde{t}-\tilde{s})+3\tilde{s}\cos(\tilde{t}-\tilde{s})\right.\\&\left.+\tilde{s}^2\sin(3(\tilde{t}-\tilde{s}))+\tilde{s}\cos(3(\tilde{t}-\tilde{s}))\right],\end{aligned} \tag{2.14}$$

$$\langle\tilde{\xi}_{\varepsilon\mu}\rangle=\langle\tilde{\xi}_{\varepsilon\varepsilon\mu}\rangle=\langle\tilde{\xi}_{\mu\mu\mu}\rangle=0, \tag{2.15}$$

$$\begin{aligned}\langle\tilde{\xi}_{\mu\mu}\rangle=&\left(\frac{\tilde{S}_L}{2}-\frac{5}{\tilde{S}_L}\right)\tilde{s}+\left(\frac{3\tilde{L}_{11}}{\tilde{S}_L^2}+\frac{\pi\tilde{s}^2}{\tilde{L}_{11}}\right)\mathrm{erf}\left(\frac{\sqrt{\pi}}{2}\frac{\tilde{S}_L\tilde{s}}{\tilde{L}_{11}}\right)\\&+\frac{2\tilde{s}}{\tilde{S}_L}\exp\left(-\frac{\pi}{4}\left(\frac{\tilde{S}_L\tilde{s}}{\tilde{L}_{11}}\right)^2\right),\end{aligned} \tag{2.16}$$

$$\langle\tilde{\xi}_{\varepsilon\mu\mu}\rangle = \left\{ \begin{array}{l} \left(-\dfrac{2}{3}\tilde{s}^2 - \dfrac{2}{3\pi}\left(\dfrac{\tilde{L}_{11}}{\tilde{S}_L}\right)^2\right)\exp\left(-\dfrac{\pi}{4}\left(\dfrac{\tilde{S}_L\tilde{s}}{\tilde{L}_{11}}\right)^2\right) \\ -\left(\dfrac{\pi}{3}\dfrac{\tilde{S}_L\tilde{s}^3}{\tilde{L}_{11}} + \dfrac{\tilde{L}_{11}\tilde{s}}{\tilde{S}_L}\right)\mathrm{erf}\left(\dfrac{\sqrt{\pi}}{2}\dfrac{\tilde{S}_L\tilde{s}}{\tilde{L}_{11}}\right) \\ \quad + \left(1 - \dfrac{1}{2}\tilde{S}_L^2\right)\tilde{s}^2 + \dfrac{2}{3\pi}\dfrac{\tilde{L}_{11}^2}{\tilde{S}_L^2} \end{array} \right\} \sin(\tilde{t} - \tilde{s}) \qquad (2.17)$$

$$+ \left\{ -4\tilde{s}\exp\left(-\frac{\pi}{4}\left(\frac{\tilde{S}_L\tilde{s}}{\tilde{L}_{11}}\right)^2\right) - \left(\frac{2\pi\tilde{S}_L\tilde{s}^2}{\tilde{L}_{11}} + \frac{\tilde{L}_{11}}{\tilde{S}_L}\right) \times \mathrm{erf}\left(\frac{\sqrt{\pi}}{2}\frac{\tilde{S}_L\tilde{s}}{\tilde{L}_{11}}\right) + 4\tilde{s} - \frac{3}{2}\tilde{S}_L^2\tilde{s}\right\}\cos(\tilde{t} - \tilde{s}). \qquad (2.18)$$

As shown in (2.15), the ensemble average of several of the terms in the expansion is zero. The terms contributing to either the ensemble or time average are $\langle\tilde{\xi}_{\varepsilon}\rangle$, $\langle\tilde{\xi}_{\varepsilon\varepsilon}\rangle$, $\langle\tilde{\xi}_{\mu\mu}\rangle$, $\langle\tilde{\xi}_{\varepsilon\varepsilon\varepsilon}\rangle$ and $\langle\tilde{\xi}_{\varepsilon\mu\mu}\rangle$. Note that the non-zero time-averaged terms reflect a shift in flame position from its unperturbed location, due to the augmentation of the turbulent burning velocity by flow fluctuations, both narrowband and stochastic. This solution is discussed further and compared with computations in the next section.

3. Results and analysis

This section presents analyses of the computational and asymptotic flame results to understand the factors controlling the ensemble-averaged dynamics of flame wrinkles. Figures 8(*a,b*) and 8(*c,d*) display a typical sequence of instantaneous computational results at two turbulence intensities. They show the presence of randomly distributed flame wrinkles with variation in both *s*- and *z*-directions; variations in the *z*-direction disappear with ensemble averaging. Also evident in the images is the progressive decay in the coherent, sinuous flame sheet fluctuations with downstream distance, as discussed in § 1. As we will show in this section, these wrinkles decay even in the absence of turbulence, but the decay rate is accelerated by turbulent fluctuations.

3.1. *Ensemble-averaged near-field characteristics*

This section presents results illustrating the role of turbulent fluctuations in smoothing the excited flame wrinkles near the flame holder, where the asymptotic results can also be used. These results are a generalization of those shown in figure 4, that illustrated the role of kinematic restoration in evolving the flame wrinkle shape in a laminar flow.

Figure 9(*a*) plots the ensemble-averaged flame position at four phases during a forcing period. For reference, the laminar case (i.e. $\tilde{\mu} = 0$) is also indicated by the dashed lines. Several observations can be made from this. First, it shows that harmonically oscillating flame wrinkles convect downstream while decaying as damped sinusoids. Second, note that the overall turbulent flame position shifts upward relative to the laminar one with downstream distance, due to the increase of the turbulent burning velocity by the random fluctuations (Hemchandra & Lieuwen 2010). Third, the ensemble average of the turbulent case shows a smoothing of the trailing edges, in contrast to the discontinuity in slope that occurs in the constant-burning-velocity,

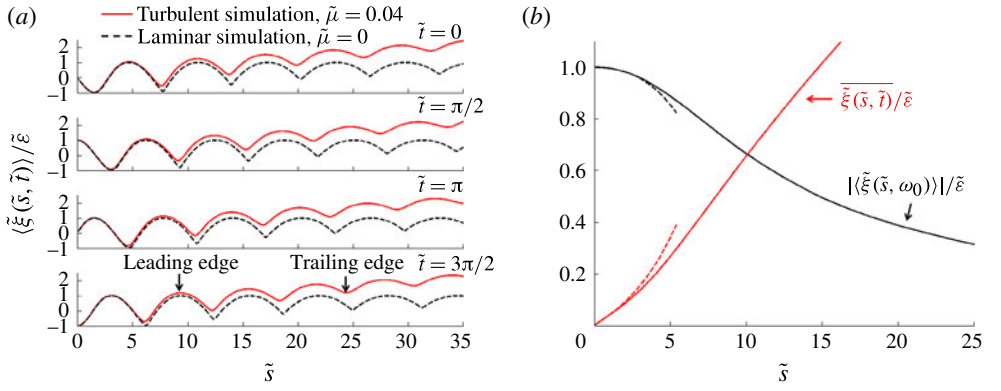

FIGURE 9. (Colour online) (*a*) Ensemble-averaged flame position, $\langle\tilde{\xi}(\tilde{s}, \tilde{t})\rangle$, at four times during a forcing period obtained from level-set computations, and compared to the laminar case ($\tilde{\mu} = 0$). (*b*) Corresponding Fourier coefficients of ensemble-averaged flame front (solid) and corresponding asymptotic solutions (dashed). Conditions are $\tilde{S}_L = 0.25$, $\tilde{\varepsilon} = 0.65$, $\tilde{\mu} = 0.04$, $\tilde{L}_{11} = 0.65$.

laminar case. This smoothing of the very short-wavelength trailing edge resembles the effect of stretch in laminar flames with positive Markstein lengths, an observation that will be quantified and fleshed out later. Finally, the peak-to-peak amplitude of the flame wrinkle is clearly different between the two curves, showing the accelerating smoothing of the flame wrinkle in the turbulent case.

These observations are further quantified in figure 9(*b*), which plots the axial dependence of the ensemble-averaged flame response at the forcing frequency, ω_0, and the time-averaged position. The figure shows the monotonic decay in flame wrinkle amplitude, as well as the shift outward in average flame position, due to the rise in turbulent burning velocity. The asymptotic solutions, presented in (2.13)–(2.17) are also indicated in figure 9(*b*) by the dashed lines, which show good agreement in the near field. These asymptotic solutions can be interpreted more easily by being expanded in powers of tangential coordinate, $\tilde{s}$, as:

$$\overline{\tilde{\xi}(\tilde{s}, \tilde{t})} = \tilde{\mu}^2 \left(\frac{\tilde{S}_L}{2}\tilde{s} + \frac{\pi}{4}\frac{\tilde{S}_L}{\tilde{L}_{11}^2}\tilde{s}^3 + O(\tilde{s}^5) \right) + \frac{1}{4}\tilde{\varepsilon}^2\tilde{S}_L\tilde{s} + O((\tilde{\mu}, \tilde{\varepsilon})^4), \quad (3.1)$$

$$\frac{|\langle\tilde{\xi}(\tilde{s}, \omega_0)\rangle|}{\tilde{\varepsilon}} = 1 - \frac{1}{8}\tilde{\varepsilon}^2\tilde{S}_L^2\tilde{s}^2 - \frac{1}{2}\tilde{\mu}^2\tilde{s}^2 - \frac{1}{2}\tilde{\mu}^2\tilde{S}_L^2\tilde{s}^2 - \frac{5\pi}{48}\frac{\tilde{\mu}^2\tilde{S}_L^2}{\tilde{L}_{11}^2}\tilde{s}^4 + O(\tilde{s}^5, \tilde{\mu}^3), \quad (3.2)$$

where the overbar represents the time average. Note that the second term on the right-hand side of (3.2) describes the decrease in laminar flame wrinkle size due to kinematic restoration, which was presented in Shin & Lieuwen (2012). We will next focus on the remaining terms that are multiplied by $\tilde{\mu}^2$ and, thus, are due to stochastic forcing effects. This equation shows that the flame wrinkle size decays quadratically with downstream distance, $\tilde{s}^2$, and turbulence intensity, $\tilde{\mu}^2$, in the near field. There are two terms, $-\tilde{\mu}^2\tilde{s}^2/2$ and $-\tilde{\mu}^2\tilde{S}_L^2\tilde{s}^2/2$, due to two fundamentally different processes leading to this smoothing effect in the leading-order terms. The first of these terms, $-\tilde{\mu}^2\tilde{s}^2/2$, is independent of burning velocity or equivalently, kinematic restoration

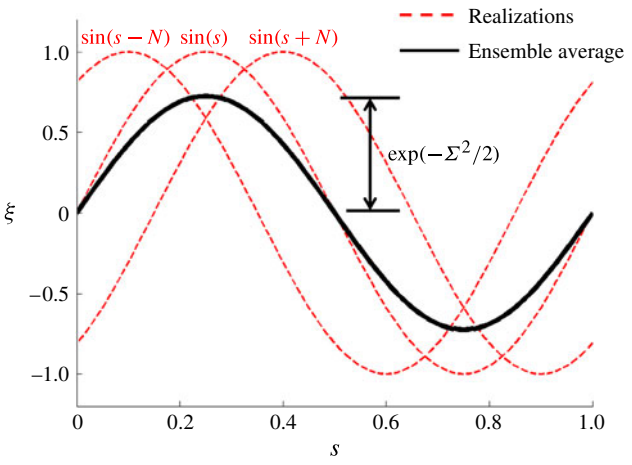

FIGURE 10. (Colour online) Illustration of the reduction of ensemble-averaged flame wrinkle size by random tangential motions of the flame wrinkle, or 'phase jitter'.

effects. Since, $\tilde{S}_L \ll 1$ in high-velocity flows, this term is actually the dominant near-field effect for the turbulent flow field used in this study.

This dominant smoothing effect $(-\tilde{\mu}^2\tilde{s}^2/2)$ is due to phase jitter associated with the $\mu f_s\, \partial\xi/\partial s$ term on the right side of (2.4); i.e. fluctuations in tangential flow velocity cause the axial position of the flame wrinkle to fluctuate randomly. As shown in figure 10, this leads to a reduction in ensemble-averaged flame wrinkle amplitude, as the ensemble average of a harmonic quantity subjected to phase jitter is reduced in magnitude.

To illustrate, consider the ensemble average of a harmonically oscillating disturbance, $\sin(2\pi s)$, subjected to a Gaussian phase noise, $N(t)$, with a mean of zero and a variance of Σ^2. The ensemble average of the disturbance is written as:

$$\langle \sin(2\pi s + N(t))\rangle = \sin(2\pi s)\,\langle \cos(N(t))\rangle + \cos(2\pi s)\,\langle \sin(N(t))\rangle. \tag{3.3}$$

Note that $\langle \cos(N(t))\rangle = \exp(-\Sigma^2/2)$ and $\langle \sin(N(t))\rangle = 0$ for Gaussian noise. Therefore, (3.3) becomes:

$$\langle \sin(2\pi s + N(t))\rangle = \exp(-\Sigma^2/2)\ \sin(2\pi s). \tag{3.4}$$

This equation indicates that the ensemble average of the disturbance decreases exponentially in magnitude with increases in variance, Σ^2, of the noise. Note that this effect is only due to tangential velocity fluctuations, u_s'. In contrast, velocity fluctuations normal to the flame, u_n', do not alter the ensemble average by convection effects. This is analogous to additive noise addition to a harmonic disturbance:

$$\langle \sin(2\pi s) + N(t)\rangle = \sin(2\pi s). \tag{3.5}$$

Related phase jitter effects have been well documented in the general turbulent flow and flame literature (Cardell 1993; Coats 1996; Shanbhogue, Seelhorst & Lieuwen 2009*b*).

Returning to (3.2), consider the next quadratic term, $-\tilde{\mu}^2\tilde{S}_L^2\tilde{s}^2/2$. The fact that it is proportional to $\tilde{\mu}\tilde{S}_L$ indicates that it is influenced by kinematic restoration and stochastic forcing, but note that it is completely independent of turbulent length scale, $\tilde{L}_{11}$. This term reflects the effects of random flame angle changes at the attachment

point by the stochastic velocity fluctuation normal to the front. To see this, note that the kinematic restoration term in (2.4) can be rewritten as $(S_L/\cos\theta(t) - S_L)$ by using the equality $\sqrt{1+(\partial\xi/\partial s)^2+(\partial\xi/\partial z)^2} = 1/\cos\theta(t)$, where $\theta(t)$ is the instantaneous local flame angle measured relative to the s–z plane. Since the flame angle (θ) consists of deterministic (θ_D) and random (θ_N) parts, i.e. $\theta = \theta_D + \theta_N$, the kinematic restoration effect is expanded for small θ_D and θ_N as:

$$\frac{S_L}{\cos(\theta_D+\theta_N)} - S_L = S_L\ (\theta_D+\theta_N)^2/2 + O((\theta_D,\theta_N)^3). \tag{3.6}$$

Ensemble averaging this expression:

$$\left\langle \frac{S_L}{\cos(\theta_D+\theta_N)} - S_L \right\rangle = \frac{S_L\theta_D^2}{2} + \frac{S_L\langle\theta_N^2\rangle}{2} + O((\theta_D,\theta_N)^3). \tag{3.7}$$

This equation indicates the leading-order effects of kinematic restoration. The first term, $S_L\theta_D^2/2$, is the laminar kinematic restoration term, corresponding to $-\tilde{\varepsilon}^2\tilde{S}_L^2\tilde{s}^2/8$ in (3.2). Similarly, the second term, $S_L\langle\theta_N^2\rangle/2$, corresponds to $-\tilde{\mu}^2\tilde{S}_L^2\tilde{s}^2/2$ in (3.2).

Lastly, kinematic restoration effects associated with random wrinkles excited in the domain itself first appear in the expansion (3.2) at fourth-order in distance, but second-order in turbulence intensity, through the term $(5\pi/48)(\tilde{\mu}^2\tilde{S}_L^2/\tilde{L}_{11}^2)\tilde{s}^4$. Note that this includes terms proportional to $\tilde{S}_L$ and $\tilde{L}_{11}$, indicating that it is influenced by kinematic restoration and turbulence length scale. This is the leading-order near-field term describing the turbulent destruction of wrinkles in the domain itself. It shows that turbulent fluctuations of shorter length scale lead to more rapid dissipation of flame wrinkles, scaling as $1/\tilde{L}_{11}^2$, an effect which would be expected given the scale-dependent nature of kinematic restoration.

This asymptotic expansion shows how three fundamentally different effects come into play in the near field, with completely different dependences on location (e.g. $\tilde{s}^2$ or $\tilde{s}^4$), flame propagation (e.g. 1 or $\tilde{S}_L^2$), and turbulence characteristics (e.g. $\tilde{L}_{11}$). However, as shown in figure 9(*b*), this expansion loses validity with downstream distance, $\tilde{s} > \sim 3$ in this example, where the coupled effects of kinematic restoration and stochastic excitation must be studied numerically.

An additional important result from the asymptotic analysis is that the deterministic and stochastic effects are decoupled up to third-order, as $\langle\tilde{\xi}_{\varepsilon\varepsilon\mu}\rangle = 0$ in (2.15). As a result, to this order, the leading-order correction to the flame response can be obtained from the following linear sum of deterministic and stochastic effects in isolation:

$$\text{near field}: \quad \frac{|\langle\tilde{\xi}(\tilde{s},\omega_0)\rangle|}{\tilde{\varepsilon}} = 1 - \frac{1}{8}(\tilde{\varepsilon}\tilde{S}_L\tilde{s})^2 - \frac{\tilde{\mu}^2}{2}(1+\tilde{S}_L^2)\tilde{s}^2 + O(\tilde{s}^4,(\tilde{\varepsilon},\tilde{\mu})^4). \tag{3.8}$$

However, this result is limited to the near field as the asymptotic solution in (2.15)–(2.17) quickly loses accuracy further downstream.

In order to illustrate the combined effects of harmonic and stochastic excitation, figure 11 plots the results of several computations showing the axial dependence of the flame wrinkle fluctuation amplitude at the forcing frequency at several turbulence intensities. The $\tilde{\mu} = 0$ curve shows the laminar result, showing the monotonic decay in flame wrinkle amplitude with downstream distance, for reasons discussed previously. In addition, curves are shown for $\tilde{\mu} = 0.04$ and 0.10, showing the increased decay rate of $|\langle\tilde{\xi}(\tilde{s},\omega_0)\rangle|$ with increasing turbulence intensity. The plot clearly shows how

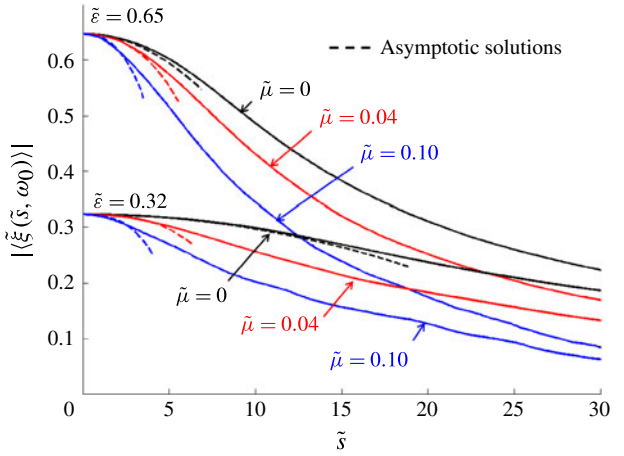

FIGURE 11. (Colour online) Comparison of the flame responses at different turbulence intensities and two different forcing amplitudes ($\tilde{S}_L = 0.25$ and $\tilde{L}_{11} = 0.65$).

both deterministic and stochastic processes lead to a decay in flame wrinkle size. Their relative significance is a function of the values of $\tilde{\varepsilon}$ and $\tilde{\mu}$.

The rest of this paper considers these downstream characteristics in more detail. In order to understand the factors controlling the far-field region, it is first necessary to understand the effects of stochastic forcing on the ensemble-averaged, time-varying turbulent burning velocity, which is treated next.

3.2. *Ensemble-averaged turbulent burning velocity*

In the laminar case, it is the propagation of the flame normal to itself that leads to smoothing of flame wrinkles, as illustrated in figure 4; thus the wrinkle decay rate is directly proportional to the laminar burning velocity, S_L, as shown in (1.2). Important insights into the turbulent case can be obtained by considering analogies to the laminar problem and considering the ensemble-averaged turbulent burning velocity. An important generalization from the laminar problem, however, is that even in the case where the flame has no stretch sensitivity, the turbulent burning velocity is time varying and modulated harmonically.

To follow this point, consider an equation for the ensemble-averaged flame dynamics, motivated in form by the actual level-set equation (2.2) (this expression is similar to those proposed heuristically in prior studies, e.g. Lipatnikov & Sathiah 2005; Palies *et al.* 2011; Shin *et al.* 2011):

$$\frac{\partial\langle\tilde{\xi}\rangle}{\partial\tilde{t}} + \langle\tilde{u}_s\rangle\frac{\partial\langle\tilde{\xi}\rangle}{\partial\tilde{s}} - \langle\tilde{u}_n\rangle + \langle\tilde{u}_z\rangle\frac{\partial\langle\tilde{\xi}\rangle}{\partial\tilde{z}} = \tilde{S}_{T,eff}\left[1 + \left(\frac{\partial\langle\tilde{\xi}\rangle}{\partial\tilde{s}}\right)^2 + \left(\frac{\partial\langle\tilde{\xi}\rangle}{\partial\tilde{z}}\right)^2\right]^{1/2}, \quad (3.9)$$

where $(\tilde{\ })$ represents a non-dimensional variable defined as in (2.8) – velocities, lengths, and time are normalized by $u_{s,0}$, $u_{s,0}/\omega_0$ and ω_0, respectively. Note that this equation is not derived by ensemble averaging (2.2), as nonlinear terms lead to similar closure problems as arise in Reynolds time-averaging the Navier–Stokes equation. Rather, this equation is essentially a definition for the ensemble-averaged

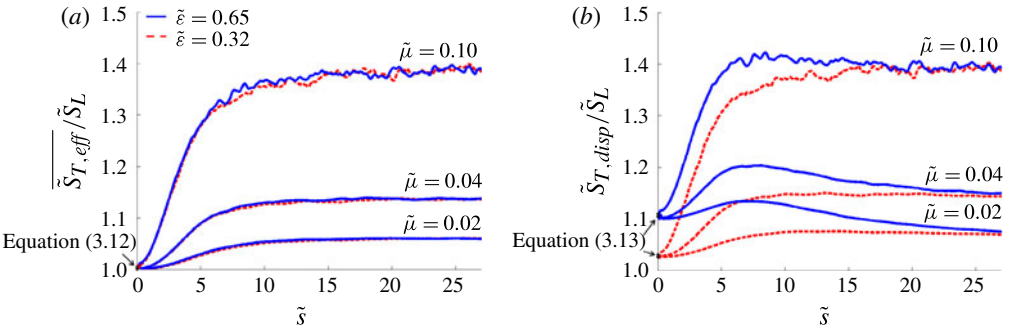

FIGURE 12. (Colour online) Dependence of (*a*) $\overline{\tilde{S}_{T,eff}}$ and (*b*) $\tilde{S}_{T,disp}$ on downstream distance for the same intensities and amplitudes as in figure 11 ($\tilde{S}_L = 0.25$ and $\tilde{L}_{11} = 0.65$).

turbulent burning velocity, $\tilde{S}_{T,eff}$, obtained by rearranging (3.9) as:

$$\tilde{S}_{T,eff}(\tilde{s},\tilde{z},\tilde{t}) \equiv \frac{\dfrac{\partial\langle\tilde{\xi}\rangle}{\partial\tilde{t}} + \langle\tilde{u}_s\rangle\dfrac{\partial\langle\xi\rangle}{\partial\tilde{s}} - \langle\tilde{u}_n\rangle + \langle\tilde{u}_z\rangle\dfrac{\partial\langle\tilde{\xi}\rangle}{\partial\tilde{z}}}{\left[1 + \left(\partial\langle\tilde{\xi}\rangle/\partial\tilde{s}\right)^2 + \left(\partial\langle\tilde{\xi}\rangle/\partial\tilde{z}\right)^2\right]^{1/2}}. \tag{3.10}$$

It is important to note that the turbulent flame speed can be defined in different ways for this problem, leading to different results. The typical definition of displacement flame speed, $\tilde{S}_{T,disp}$, used in flows without harmonic forcing is (Driscoll 2008):

$$\tilde{S}_{T,disp}(\tilde{s},\tilde{z}) \equiv \frac{\bar{\tilde{u}}_s\,\partial\bar{\tilde{\xi}}/\partial\tilde{s} - \bar{\tilde{u}}_n + \bar{\tilde{u}}_z\,\partial\bar{\tilde{\xi}}/\partial\tilde{z}}{[1 + (\partial\bar{\tilde{\xi}}/\partial\tilde{s})^2 + (\partial\bar{\tilde{\xi}}/\partial\tilde{z})^2]^{1/2}}. \tag{3.11}$$

The time average of $\tilde{S}_{T,eff}$, $\overline{\tilde{S}_{T,eff}}$, differs from $\tilde{S}_{T,disp}$ because of the non-zero time average produced by the multiplication of two harmonically oscillating terms. For example, $\overline{\bar{\tilde{u}}_s}\,\partial\bar{\tilde{\xi}}/\partial\tilde{s}$ does not equal $\overline{\tilde{u}_s\,\partial\bar{\tilde{\xi}}/\partial\tilde{s}}$ in the presence of harmonic flow perturbations. This difference can be explicitly shown from the asymptotic solutions for $\overline{\tilde{S}_{T,eff}}$ and $\tilde{S}_{T,disp}$ at $\tilde{s} = 0$:

$$\frac{\overline{\tilde{S}_{T,eff}}(\tilde{s}=0)}{\tilde{S}_L} = 1 + \frac{\tilde{\mu}^2}{2} + O((\tilde{\varepsilon},\tilde{\mu})^4), \tag{3.12}$$

$$\frac{\tilde{S}_{T,disp}(\tilde{s}=0)}{\tilde{S}_L} = 1 + \frac{1}{4}\tilde{\varepsilon}^2 + \frac{1}{2}\tilde{\mu}^2 + O((\tilde{\varepsilon},\tilde{\mu})^4). \tag{3.13}$$

Note that these equations converge to the same result when $\tilde{\varepsilon} = 0$, but otherwise, $\tilde{S}_{T,disp}$ has an $\tilde{\varepsilon}$ sensitivity while $\overline{\tilde{S}_{T,eff}}$ does not. Similar points can be seen more generally in figure 12(*a*,*b*), which plots the computed dependence of $\overline{\tilde{S}_{T,eff}}$ and $\tilde{S}_{T,disp}$ upon downstream distance, $\tilde{s}$, for different $\tilde{\varepsilon}$ and $\tilde{\mu}$ values.

At a fixed axial location, both $\overline{\tilde{S}_{T,eff}}$ and $\tilde{S}_{T,disp}$ are an increasing function of $\tilde{\mu}$, as might be expected. However, $\overline{\tilde{S}_{T,eff}}$ is essentially independent of harmonic forcing

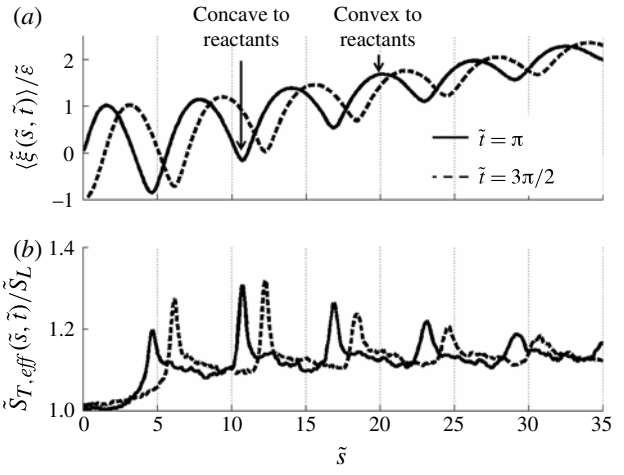

FIGURE 13. Dependence of ensemble-averaged flame position (a) and extracted $\tilde{S}_{T,eff}$ value (b) on downstream distance at two time instants ($\tilde{S}_L = 0.25$, $\tilde{\varepsilon} = 0.65$, $\tilde{L}_{11} = 0.65$, $\tilde{\mu} = 0.04$).

amplitude, $\tilde{\varepsilon}$, for all cases shown, as suggested by (3.12). As shown later, $\tilde{S}_{T,eff}$ does vary in time, however, as it is modulated by the harmonic forcing.

Having discussed some basic differences from typical definitions used in the turbulent combustion literature in the absence of harmonic forcing, we next consider its characteristics further. The space–time dependence of $\overline{\tilde{S}_{T,eff}}$ can be directly extracted from computed results using (3.10). To illustrate, figure 13 plots the extracted dependence of $\tilde{S}_{T,eff}$ at two time instants for the calculation shown in figure 9(a), where the instantaneous flame position is also plotted for ease of comparison.

This figure shows that $\tilde{S}_{T,eff}$ is a function of both space and time. The rest of this section briefly revisits its time-averaged characteristics, and then focuses on its time-varying features. The axial evolution of $\overline{\tilde{S}_{T,eff}}$ shown in figure 12(a) indicates an initial development in the near field followed by saturation far from the flame holder, similar to other observations in spatially or temporally evolving flames (Abdel-Gayed, Bradley & Lawes 1987; Lipatnikov & Chomiak 2002). The fact that $\overline{\tilde{S}_{T,eff}}$ exceeds $\tilde{S}_L$, such as shown in figure 12, is important and directly responsible for the increasing decay rate of flame wrinkles shown in figure 11. The results in figure 11 show that increasing $\tilde{\mu}$ at a fixed $\tilde{\varepsilon}$ leads to a monotonically increasing rate at which flame wrinkles are smoothed out. In other words, a faster average burning rate leads to faster smoothing of the ensemble-averaged flame wrinkles, directly analogous to the sensitivity of laminar flames to $\tilde{S}_L$. This point can also be seen by noting that (2.2) and (3.9) are identical if $\tilde{S}_{T,eff}$ is a constant, and replacing $\tilde{\xi}$ and $\tilde{S}_L$ with $\langle\tilde{\xi}\rangle$ and $\tilde{S}_{T,eff}$, respectively.

Having considered the effects of $\overline{\tilde{S}_{T,eff}}$ upon the decay rate of flame wrinkles, we next consider its space–time modulation, illustrated in figure 13. In comparing figures 13(a) and 13(b) note how $\tilde{S}_{T,eff}$ instantaneously rises at points where the ensemble-averaged front is concave to the reactants and falls at points that are convex. This point is quantified in figure 14(a) which plot values of $\tilde{S}_{T,eff}$ extracted from calculations at points through the harmonic forcing cycle, as a function of ensemble-

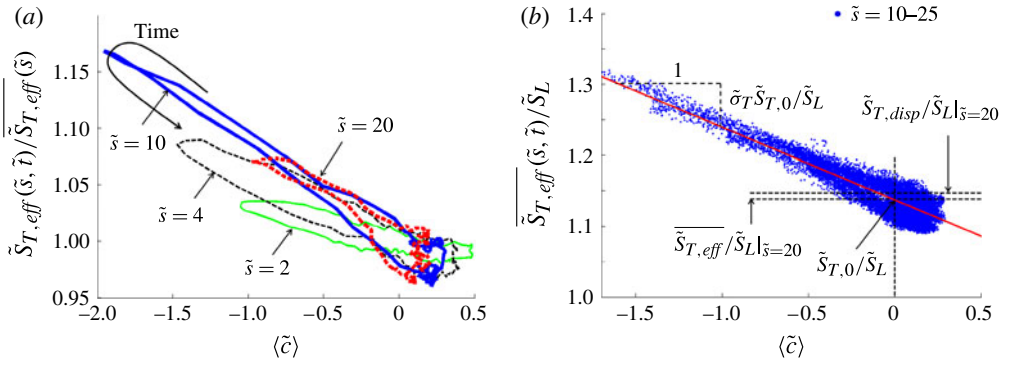

FIGURE 14. (Colour online) Correlation of the curvature of the ensemble-averaged flame front and the turbulent flame speed defined in (3.9): (*a*) scaled by $\overline{\tilde{S}_{T,eff}}(\tilde{s})$ at selected downstream locations and (*b*) scaled by the laminar flame speed at downstream locations where $\overline{\tilde{S}_{T,eff}}$ has approached a constant value. Values of $\overline{\tilde{S}_{T,eff}}/\tilde{S}_L|_{\tilde{s}=20}$, $\tilde{S}_{T,disp}/\tilde{S}_L|_{\tilde{s}=20}$, $\tilde{S}_{T,0}/\tilde{S}_L$ and $\tilde{\sigma}_T\tilde{S}_{T,0}/\tilde{S}_L$ are indicated for reference, and are 1.14, 1.15, 1.14 and −0.102, respectively (conditions are $\tilde{\varepsilon}=0.65$, $\tilde{\mu}=0.04$, $\tilde{L}_{11}=0.65$, $\tilde{S}_L=0.25$).

averaged radius of curvature of the flame, $\langle\tilde{c}\rangle$, defined as:

$$\langle\tilde{c}\rangle=\frac{\partial^2\langle\tilde{\xi}(\tilde{s},\tilde{t})\rangle/\partial\tilde{s}^2}{[1+(\partial\langle\tilde{\xi}(\tilde{s},\tilde{t})\rangle/\partial\tilde{s})^2]^{3/2}}. \tag{3.14}$$

Note the clear negative correlation of burning velocity with ensemble-averaged curvature. In other words, locations with ensemble-averaged negative curvatures are associated with augmentation of the unsteady, ensemble-averaged burning velocity and vice-versa. This behaviour is analogous to stretch-sensitive flames with positive Markstein lengths; i.e. where $\sigma>0$. In the laminar case, this stretch sensitivity is due to convective–diffusive flux imbalances in the finite-thickness flame (Matalon 1983), while the analogous behaviour in the turbulent case is due to the effect of stochastic flame wrinkling on the ensemble-averaged flame wrinkle position. However, it is important to emphasize that while the Markstein length concept applies instantaneously in the laminar case, this turbulent analogue applies only to the ensemble average.

The fact that the curves trace out an ellipse suggests that the relationship between instantaneous curvature and $\tilde{S}_{T,eff}$ is not quasi-steady; i.e. there is a phase lag between the two, but this lag is not large for this condition. Note also how the $\tilde{S}_{T,eff}$ and $\langle\tilde{c}\rangle$ correlation becomes nearly independent of position at $\tilde{s}=10$ and 20, which corresponds to locations where $\overline{\tilde{S}_{T,eff}}$ has approached a constant value.

For the rest of this section, we focus on this relationship at downstream locations where $\overline{\tilde{S}_{T,eff}}$ is approximately spatially constant. Figure 14(*b*) plots $\tilde{S}_{T,eff}$ at a range of such positions, showing that we can write the following approximate expression for $\tilde{S}_{T,eff}$ in the far field:

$$\tilde{S}_{T,eff}=\tilde{S}_{T,0}(1-\tilde{\sigma}_T\langle\tilde{c}\rangle), \tag{3.15}$$

where $\tilde{S}_{T,0}$ and $\tilde{\sigma}_T$ are the effective turbulent flame speed at zero curvature and the 'turbulent Markstein length', respectively. This effect of global curvature on the

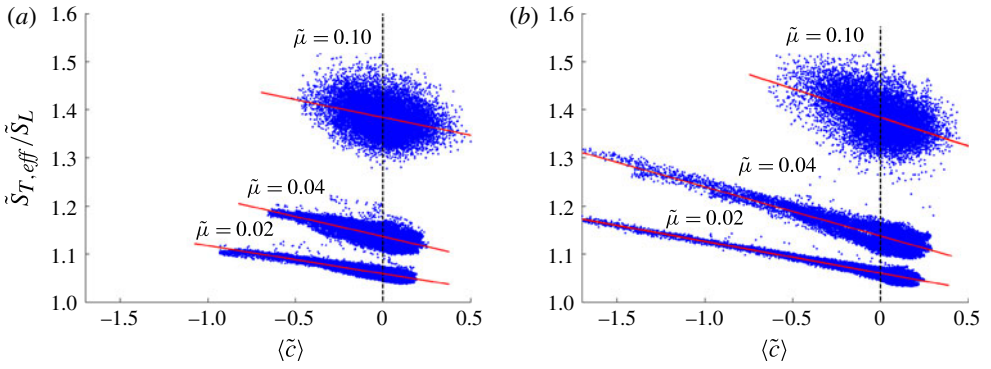

FIGURE 15. (Colour online) Correlation of the curvature of the ensemble-averaged flame front and the turbulent flame speed defined in (3.9). (*a*) $\tilde{\varepsilon} = 0.32$; (*b*) $\tilde{\varepsilon} = 0.65$ (other conditions are $\tilde{L}_{11} = 0.65$, $\tilde{S}_L = 0.25$).

turbulent burning velocity has been previously discussed in spherically expanding flame studies in a turbulent flow field (Lipatnikov & Chomiak 2004). They showed that with increasing time/flame radius, the turbulent flame speed increases. Other studies suggest that this effect is due to the increasing range of wrinkling scale sizes, and therefore flame surface area (Abdel-Gayed *et al.* 1987; Groff 1987). In addition, Lipatnikov & Chomiak (2007) analysed the characteristics of a curved turbulent flame using the Reynolds-averaged progress variable equation and the closure model from Zimont & Lipatnikov (1995) (a model developed from Prudnikov 1964; Zimont 1977). They showed that the turbulent burning velocity was curvature dependent in that formulation as well. They denoted the burning velocity curvature sensitivity coefficient as the 'turbulent Markstein length', noting its analogy to the Markstein length for laminar flamelets. In their analysis, this curvature sensitivity is proportional to the gas expansion across the flame.

Note that $\tilde{S}_{T,0}$ and $\overline{\tilde{S}_{T,eff}}$ have different definitions in general, but are similar in value as shown by figure 14(*b*). Also, a more accurate representation of the ensemble-averaged burning velocity would be to include the phase delay between $\tilde{S}_{T,eff}$ and $\langle\tilde{c}\rangle$, which we will not do here for simplicity. A more detailed characterization of the effects of harmonic modulation on $\tilde{S}_{T,eff}$ is outside the scope of this study.

The same behaviour was observed for all computed cases. To illustrate, figure 15 plots similar calculation results for several turbulence intensities, showing that $\tilde{\sigma}_T$ is an increasing function of turbulence intensity, as might be expected. The larger scatter in the $\tilde{\mu} = 0.1$ case is likely a reflection of noise introduced in calculation of the second derivative of flame position, needed for the curvature. Although the 160 ensemble averages are sufficient for calculation of $\langle\tilde{\xi}\rangle$, the small amount of noise present in these ensemble average estimates is amplified significantly in estimates of the second derivative. Results are shown for two $\tilde{\varepsilon}$ values, showing the larger range of ensemble-averaged flame curvatures that are present with increased harmonic forcing amplitude. Note also the diminished range of negative curvature values for the highest $\tilde{\mu}$ case, a reflection of the very rapid destruction of high-curvature regions by stochastic flame wrinkling.

While the Markstein length analogy has been quantified in figure 14 based on post-processing calculations, the physical reasons why this behaviour occurs can

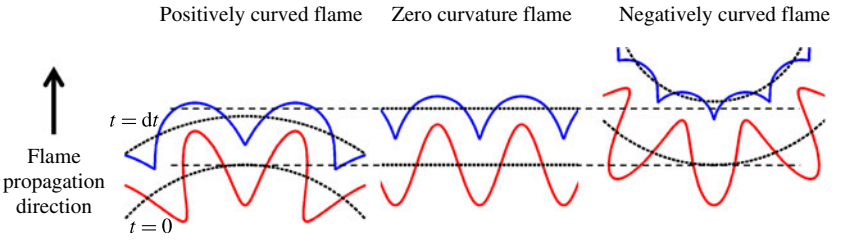

FIGURE 16. (Colour online) Illustration of change of curvatures on trailing edges of the flames with different large-scale curvatures (solid lines: instantaneous flame front, thick dotted lines: space-averaged flame front).

be understood from consideration of Huygens propagation. To illustrate, figure 16 illustrates three instantaneous notational images of flames with ensemble-averaged positive, negative, and zero curvatures with superposed wrinkles from $t = 0$ to $\mathrm{d}t$. The solid lines denote instantaneous flame fronts, while the thick dotted lines are spatially averaged flame fronts.

As shown in figure 16, the effect of kinematic restoration is most prominent at the trailing edges of the flame, where the two opposing flame branches propagate into each other and annihilate each other. As the trailing edges are destroyed, the averaged flame position shifts toward the reactants sides, which also manifests itself as an increase in the turbulent displacement speed; i.e. the distance between two dotted lines is proportional to the turbulent displacement speed, which is larger than the laminar flame speed. Similarly, the interaction of opposing flame branches is reduced for fronts with positive ensemble-averaged curvature, a point that can also be seen from application of Huygens propagation as shown in figure 3.

This flame–flame interaction and annihilation process is strongly dependent upon the ensemble-averaged curvature of the flame, as it is suppressed in outwardly propagating, positively curved flames (see the different degrees of change of mean flame position from $t = 0$ to $t = \mathrm{d}t$ marked by dashed lines in figure 16). It is augmented in inwardly propagating, negatively curved flames.

To summarize then, $\tilde{S}_{T,eff}$ can be written as $\tilde{S}_{T,eff} = \overline{\tilde{S}_{T,eff}} + \tilde{S}'_{T,eff}$, where $\tilde{S}'_{T,eff}$ is a periodic function of time, that can also be approximately parameterized as a function of the local curvature, i.e.

$$\tilde{S}_{T,eff} = \overline{\tilde{S}_{T,eff}}(1 - \tilde{\sigma}_T \langle\tilde{c}\rangle). \tag{3.16}$$

Following from the analogies of the solution to the laminar flame problem, this latter effect has a term that is *linear* in harmonic perturbation amplitude, $|\langle\tilde{\xi}(\tilde{s}, \omega_0)\rangle|$; i.e. expanding the curvature in (3.14) in a Taylor series, the leading-order term is given by $\langle\tilde{c}\rangle = \partial^2\langle\tilde{\xi}(\tilde{s}, \omega_0)\rangle/\partial s^2 + O(\langle\tilde{\xi}(\tilde{s}, \omega_0)\rangle^2)$. This point has important implications for the functional dependence of $\tilde{\xi}$ upon downstream distance, as elaborated in the next section.

3.3. *Ensemble-averaged far-field characteristics*

In this section, we analyse the flame response in the far field, using results from the level-set computations. Figure 11 clearly shows the faster smoothing of ensemble-averaged flame wrinkles in the far field with increasing $\tilde{\mu}$ values. As discussed in the context of figure 12, this observation is expected based upon the increasing

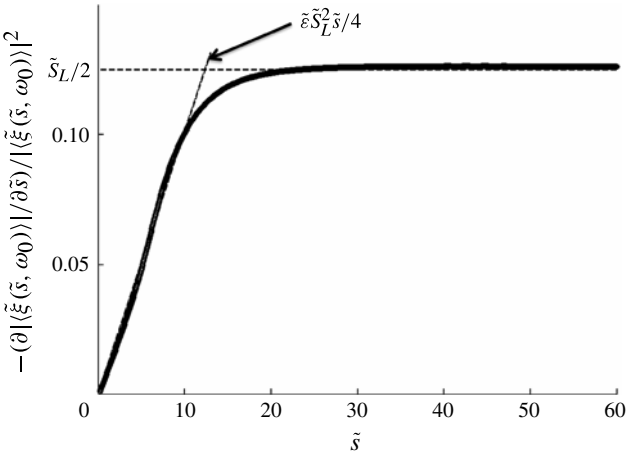

FIGURE 17. Downstream dependence of scaled slope in flame position, illustrating laminar flame scaling (conditions are $\tilde{\varepsilon} = 0.65$, $\tilde{\mu} = 0$ and $\tilde{S}_L = 0.25$).

value of $\overline{S_{T,eff}}$ with turbulence intensity, leading to faster propagation of the ensemble-averaged flame front normal to itself.

While this qualitative behaviour is expected, we can use the results from § 3.2 to better understand the functional dependence of $|\langle\tilde{\xi}(\tilde{s},\omega_0)\rangle|$ upon downstream distance. To illustrate, we briefly return to the laminar flame problem where, as discussed in § 1, two processes lead to flame wrinkle decay: kinematic restoration and flame stretch.

Consider first the decay rate of laminar flames dominated by kinematic restoration effects, using the $\tilde{s} \gg 1$ solution from (1.2). This equation can be differentiated and rewritten in the following form that eliminates the explicit dependence on downstream distance:

$$\frac{\partial|\tilde{\xi}(\tilde{s},\omega_0)|}{\partial\tilde{s}} = -\frac{\tilde{S}_L}{2}|\tilde{\xi}(\tilde{s},\omega_0)|^2. \tag{3.17}$$

This equation quantifies the decay rate in flame wrinkle amplitude in terms of the local magnitude, showing that the ratio, $-((\partial|\tilde{\xi}(\tilde{s},\omega_0)|/\partial\tilde{s})/|\tilde{\xi}(\tilde{s},\omega_0)|^2)$, reaches a constant value in the far field, where this expression is valid. To illustrate, figure 17 plots the results of a calculation for $\tilde{\mu} = 0$, i.e. a laminar flame, confirming this result. This plot also indicates that this ratio varies with distance in the near field due to the two-zone behaviour of a laminar flame as pointed out earlier ((1.2) indicates that it varies as $\tilde{\varepsilon}\tilde{S}_L^2\tilde{s}/4$).

In a similar manner, the decay rate of stretch-dominated laminar flames can be obtained from (1.3) and written as:

$$\frac{\partial|\tilde{\xi}(\tilde{s},\omega_0)|}{\partial\tilde{s}} = -\tilde{\sigma}\tilde{S}_L|\xi(\tilde{s},\omega_0)|. \tag{3.18}$$

Therefore, this ratio is proportional to the product of the flame speed and normalized Markstein length, $\tilde{\sigma}$.

These laminar solutions can be used to understand the functional dependence of $\partial|\langle\tilde{\xi}(\tilde{s},\omega_0)\rangle|/\partial\tilde{s}$ upon $|\langle\tilde{\xi}(\tilde{s},\omega_0)\rangle|$, since the laminar instantaneous and ensemble-

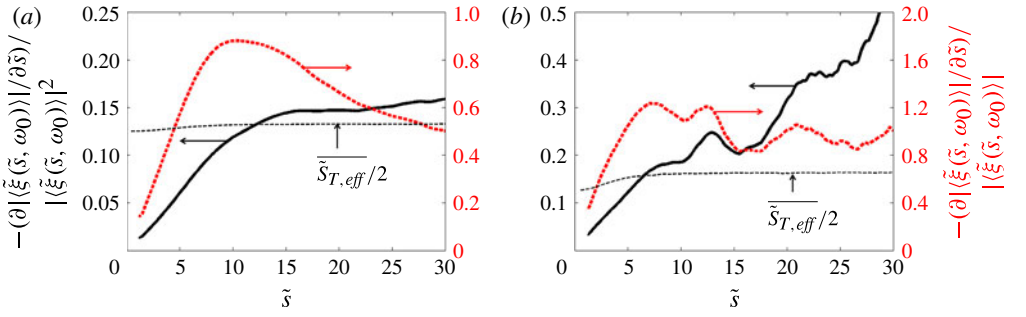

FIGURE 18. (Colour online) Ratios of ensemble-averaged flame slope and position, using two different scalings derived from kinematic restoration and stretch-dominated solutions. (*a*) $\tilde{\mu} = 0.02$ and (*b*) $\tilde{\mu} = 0.08$ (conditions are $\tilde{\varepsilon} = 0.65$, $\tilde{S}_L = 0.25$ and $\tilde{L}_{11} = 0.65$).

averaged turbulent flame characteristics are described by analogous equations in the far field; i.e.

laminar instantaneous equation:

$$\frac{\partial\tilde{\xi}}{\partial\tilde{t}} + \tilde{u}_s\frac{\partial\tilde{\xi}}{\partial\tilde{s}} - \tilde{u}_n + \tilde{u}_z\frac{\partial\tilde{\xi}}{\partial\tilde{z}} = \tilde{S}_L(1-\tilde{\sigma}\tilde{c})\left[1+\left(\frac{\partial\tilde{\xi}}{\partial\tilde{s}}\right)^2+\left(\frac{\partial\tilde{\xi}}{\partial\tilde{z}}\right)^2\right]^{1/2}; \tag{3.19}$$

turbulent ensemble-averaged equation:

$$\frac{\partial\langle\tilde{\xi}\rangle}{\partial\tilde{t}} + \langle\tilde{u}_s\rangle\frac{\partial\langle\tilde{\xi}\rangle}{\partial\tilde{s}} - \langle\tilde{u}_n\rangle + \langle\tilde{u}_z\rangle\frac{\partial\langle\tilde{\xi}\rangle}{\partial\tilde{z}} = \overline{\tilde{S}_{T,eff}}(1-\tilde{\sigma}_T\langle\tilde{c}\rangle)\left[1+\left(\frac{\partial\langle\tilde{\xi}\rangle}{\partial\tilde{s}}\right)^2+\left(\frac{\partial\langle\tilde{\xi}\rangle}{\partial\tilde{z}}\right)^2\right]^{1/2}. \tag{3.20}$$

Increases in turbulence intensity, $\tilde{\mu}$, lead to two effects: increases in $\overline{\tilde{S}_{T,eff}}$ and the fluctuation magnitude of $\tilde{S}'_{T,eff}$, because of the increases in 'turbulent Markstein length'. Again, using the previously developed laminar flame solutions as a guide, both effects lead to destruction of flame wrinkles. However, the first effect is nonlinear in harmonic disturbance amplitude, $|\langle\tilde{\xi}(\tilde{s},\omega_0)\rangle|$, while the second has a leading-order linear term in $|\langle\tilde{\xi}(\tilde{s},\omega_0)\rangle|$. Thus, the dependence of the far-field solution characteristics upon $|\langle\tilde{\xi}(\tilde{s},\omega_0)\rangle|$ are a nonlinear function of $\tilde{\mu}$.

The increase of $\overline{\tilde{S}_{T,eff}}$ enhances the kinematic restoration process and the decay of flame wrinkles. Consider the case where $\tilde{\mu} = 0$ and $\tilde{\varepsilon}$ is non-zero. In this limit, only deterministic kinematic restoration processes lead to flame wrinkle destruction, with a decay rate that is a nonlinear function of $\tilde{\varepsilon}$, as quantified in (1.2). As $\tilde{\mu}$ increases, increases in $\overline{\tilde{S}_{T,eff}}$ augment this effect, causing even faster increases in flame wrinkle decay rate, as shown by figure 11. In order to illustrate that the same basic scaling described in (3.17) applies in the low turbulence intensity case as well, figure 18 plots the axial dependence of ratios of $-\partial|\langle\tilde{\xi}(\tilde{s},\omega_0)\rangle|/\partial\tilde{s}$ to powers of $|\langle\tilde{\xi}(\tilde{s},\omega_0)\rangle|$. In the low turbulent intensity case ($\tilde{\mu} = 0.02$ in figure 18*a*), the ratio, $-((\partial|\langle\tilde{\xi}(\tilde{s},\omega_0)\rangle|/\partial\tilde{s})/|\langle\tilde{\xi}(\tilde{s},\omega_0)\rangle|^2)$ (solid line), approaches a roughly constant value,

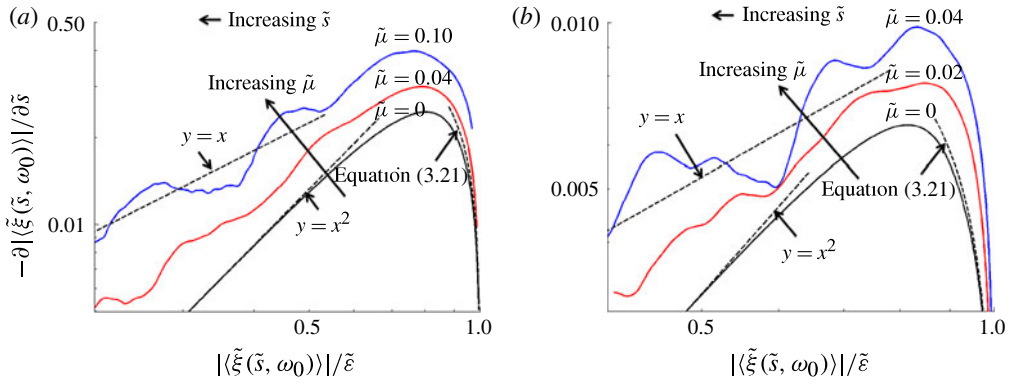

FIGURE 19. (Colour online) Relationship between local flame position and slope, illustrating transition from kinematic-restoration dominated to 'stretch'-dominated with increasing turbulence intensity. (*a*) $\tilde{\varepsilon} = 0.32$; (*b*) $\tilde{\varepsilon} = 0.65$ ($\tilde{S}_L = 0.25$ and $\tilde{L}_{11} = 0.65$).

while the ratio $-((\partial|\langle\tilde{\xi}(\tilde{s}, \omega_0)\rangle|/\partial\tilde{s})/|\langle\tilde{\xi}(\tilde{s}, \omega_0)\rangle|)$ (dashed line), continues to evolve with downstream distance. This quadratic scaling indicates that the decaying process is similar to the kinematic restoration process in laminar flames. For reference, note from figure 12(*a*) that $\overline{\tilde{S}_{T,eff}}$ approaches a spatially constant value for $\tilde{s} > \sim 10$.

However, these increases in $\tilde{\mu}$ introduce the additional modulated flame speed effect as well, an effect that, in isolation, has a completely different amplitude scaling. Moreover, this effect is also a function of $\tilde{\varepsilon}$, as larger modulations in $\langle\tilde{c}\rangle$ occur as $\tilde{\varepsilon}$ increases. This dependence of $\tilde{S}_{T,eff}$ upon ensemble-averaged curvature leads to wrinkle smoothing that is linear in $|\langle\tilde{\xi}(\tilde{s}, \omega_0)\rangle|$, as opposed to the nonlinear mechanism through which $\tilde{S}_{T,eff}$ exerts an influence. For $|\langle\tilde{\xi}(\tilde{s}, \omega_0)\rangle|/\tilde{\varepsilon} \ll 1$ then, this linear effect dominates the nonlinear effect for large enough $\tilde{\mu}$.

This linear scaling can be seen from the $\tilde{\mu} = 0.08$ result in figure 18(*b*), where the axial dependence of the ratio, $-((\partial|\langle\tilde{\xi}(\tilde{s}, \omega_0)\rangle|/\partial\tilde{s})/|\langle\tilde{\xi}(\tilde{s}, \omega_0)\rangle|^2)$ (solid line), looks quite different from figure 18(*a*). Rather than approaching a roughly constant value, it increases monotonically with downstream distance, even at locations where $\overline{\tilde{S}_{T,eff}}$ is nearly constant. In contrast, the ratio, $-((\partial|\langle\tilde{\xi}(\tilde{s}, \omega_0)\rangle|/\partial\tilde{s})/|\langle\tilde{\xi}(\tilde{s}, \omega_0)\rangle|)$ (dashed line), which would be expected to approach a constant for the 'stretch-dominated' scaling approaches a nearly constant value.

In both the $\tilde{\mu} = 0.02$ and 0.08 cases, the scaling is not perfect as increases in $\tilde{\mu}$ influence both processes. However, the basic argument can be made more precise by replotting these data. Specifically, figure 19 plots the far-field dependence of $-\partial|\langle\tilde{\xi}(\tilde{s}, \omega_0)\rangle|/\partial\tilde{s}$ upon $|\langle\tilde{\xi}(\tilde{s}, \omega_0)\rangle|$ for several $\tilde{\mu}$ values, where downstream distance is used as a parameter. Because $|\langle\tilde{\xi}(\tilde{s}, \omega_0)\rangle|$ monotonically decreases with downstream distance, axial location decreases in the positive axial direction.

In the near field, (3.17) shows that for $\tilde{\mu} = 0$, the relationship between slope and position is described by the asymptotic result from (1.2) and (3.17), which is given by:

$$\frac{\partial|\langle\tilde{\xi}(\tilde{s}, \omega_0)\rangle|}{\partial\tilde{s}} \approx \tilde{S}_L\,|\langle\tilde{\xi}(\tilde{s}, \omega_0)\rangle|^2\sqrt{(1 - |\langle\tilde{\xi}(\tilde{s}, \omega_0)\rangle|)/2}. \tag{3.21}$$

In the far field, the variation in functional dependence of $-\partial|\langle\tilde{\xi}(\tilde{s},\omega_0)\rangle|/\partial\tilde{s}$ upon $|\langle\tilde{\xi}(\tilde{s},\omega_0)\rangle|$ clearly transitions from the quadratic 'kinematic-restoration-dominated' scaling (i.e. dominated by the $\overline{\tilde{S}_{T,eff}}$ effect) to the linear-stretch-dominated scaling (i.e. dominated by the time varying $\tilde{S}'_{T,eff}$) with increases in $\tilde{\mu}$. Thus, these results show that the downstream decay of ensemble-averaged flame wrinkling in the high turbulence intensity case is dominated by the modulation in the turbulent burning velocity, a result that is analogous to that associated with smoothing of thermo-diffusively laminar flames.

4. Concluding remarks

The paper has described the relative contributions of deterministic and turbulent effects upon the ensemble-averaged dynamics of the flame front position, $\langle\xi\rangle$, with particular focus on the rate at which wrinkles excited by harmonic forcing are smoothed out and destroyed. Level-set computations and third-order perturbation analyses were used to illustrate different aspects of the problem. In the near field, asymptotic results show the three leading-order contributors, with phase jitter associated with random tangential convection of flame wrinkles being the leading-order effect.

Farther downstream, additional processes become important. First, the time-averaged turbulent burning velocity, $\overline{S_{T,eff}}$, increases with downstream distance, s, and turbulence intensity, μ. This faster average turbulent displacement speed of the front leads to increases in destruction of flame wrinkles. For example, the value of $|\langle\xi(s,\omega_0)\rangle|$ decays progressively faster with downstream distance as μ increases.

In addition, the ensemble-averaged turbulent burning velocity is modulated by the harmonic forcing, i.e. $S_{T,eff} = \overline{S_{T,eff}} + S'_{T,eff}$, with an inverse dependence upon ensemble-averaged flame curvature. This effect is analogous to positive-Markstein-length flames in the laminar flame case, but applies even to the ensemble-averaged characteristics of stretch-insensitive turbulent flames. The degree of modulation of $S_{T,eff}$ is a function of the modulation amplitude in the flame curvature and, thus, is a function of wrinkle amplitude, ε. It is also a function of turbulence intensity, μ, as the effect disappears in the laminar, $\mu = 0$, case. We show that, depending upon turbulence intensity, the far-field evolution of $\langle\xi(s,\omega_0)\rangle$ can be dominated by either $\overline{S_{T,eff}}$ or $S'_{T,eff}$. These two characteristics are analogous to those of stretch-sensitive laminar flames, whose downstream wrinkle decay rate can be controlled by either kinematic restoration or stretch effects.

An important result from this paper relates to the utilization of the level-set model in analytical and/or Reynolds-averaged simulations in turbulent flow fields. While several prior studies have utilized (3.9) in a somewhat heuristic fashion, the results of this paper show that such a description of the ensemble-averaged front dynamics can be used with an appropriate incorporation of the modulation of the turbulent burning velocity that harmonic forcing introduces.

Acknowledgements

This work was partially sponsored by the US Department of Energy under contract DE-NT0005054 (Mark Freeman, contract monitor) and the National Science Foundation under contract CBET-1235779 (Professor A. Atreya, contract monitor). The authors also thank Professor Menon at the Georgia Institute of Technology for generously allowing use of his computing cluster for turbulent flame simulations.

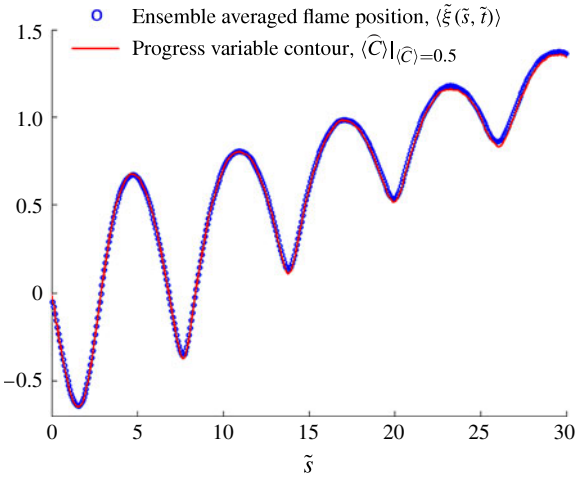

FIGURE 20. (Colour online) Comparison of ensemble average of instantaneous flame position and progress variable contour of 0.5 at one phase of the forcing period, i.e. $\tilde{t}=0$ (conditions are $\tilde{\varepsilon}=0.65$, $\tilde{\mu}=0.04$, $\tilde{S}_L=0.25$ and $\tilde{L}_{11}=0.65$).

Appendix A

From (2.6) and (2.7) the full correlation functions can be derived as:

$$R_{u_iu_j}(s_1,s_2,s_3,\tau)\equiv\frac{\langle f_i(x_1,x_2,x_3,t)f_j(x_1+s_1,x_2+s_2,x_3+s_3,t+\tau)\rangle}{\sqrt{\langle f_i^2\rangle\langle f_j^2\rangle}}$$
$$=\left(\frac{\pi}{4}\frac{\sigma_i\sigma_j}{L_{11}^2}+\left(1-\frac{\pi}{4}\left(\frac{r}{L_{11}}\right)^2\right)\delta_{ij}\right)\exp\left(-\frac{\pi}{4}\left(\frac{r}{L_{11}}\right)^2\right),\quad\text{(A 1)}$$

where $(\,)_1$: s-direction, $(\,)_2$: n-direction, $(\,)_3$: z-direction,

$$\sigma_1=s_1-u_{s,0}\tau,\quad\sigma_2=s_2+S_L\tau,\quad\sigma_3=s_3,\qquad\text{(A 2}a\text{)}$$

$$r=\sqrt{\sigma_1^2+\sigma_2^2+\sigma_3^2},\quad\delta_{ij}=\begin{cases}1 & \text{if } i=j\\ 0 & \text{otherwise.}\end{cases}\qquad\text{(A 2}b\text{)}$$

Appendix B

The progress variable, $\widehat{C}$, is defined as:

$$\widehat{C}=\begin{cases}1 & \text{in the product side}\\ 0 & \text{in the reactant side.}\end{cases}\qquad\text{(B 1)}$$

Then, $\langle\widehat{C}\rangle$ is the ensemble average of the progress variable. Figure 20 shows the comparison of the ensemble average of the flame position and 0.5-contour of ensemble-averaged progress variable, showing that they are nearly identical.

REFERENCES

ABDEL-GAYED, R., BRADLEY, D. & LAWES, M. 1987 Turbulent burning velocities: a general correlation in terms of straining rates. *Proc. R. Soc. Lond.* A **414**, 389–413.

ALDREDGE, R. C. & WILLIAMS, F. A. 1991 Influence of wrinkled premixed-flame dynamics on large-scale, low-intensity turbulent-flow. *J. Fluid Mech.* **228**, 487–511.

AYACHE, S., DAWSON, J. R., TRIANTAFYLLIDIS, A., BALACHANDRAN, R. & MASTORAKOS, E. 2010 Experiments and large-eddy simulations of acoustically forced bluff-body flows. *Intl J. Heat Fluid Flow* **31**, 754–766.

BENDAT, J. S. & PIERSOL, A. G. 2011 *Random Data: Analysis and Measurement Procedures*. Wiley.

CARDELL, G. S. 1993 *Flow Past a Circular Cylinder with a Permeable Splitter Plate*. California Institute of Technology.

COATS, C. M. 1996 Coherent structures in combustion. *Prog. Energy Combust. Sci.* **22**, 427–509.

CRETA, F., FOGLA, N. & MATALON, M. 2011 Turbulent propagation of premixed flames in the presence of Darrieus–Landau instability. *Combust. Theor. Model.* **15**, 267–298.

CRETA, F. & MATALON, M. 2011 Propagation of wrinkled turbulent flames in the context of hydrodynamic theory. *J. Fluid Mech.* **680**, 225–264.

DALLY, B. B., RIESMEIER, E. & PETERS, N. 2004 Effect of fuel mixture on moderate and intense low oxygen dilution combustion. *Combust. Flame* **137**, 418–431.

DOWLING, A. P. 1999 A kinematic model of a ducted flame. *J. Fluid Mech.* **394**, 51–72.

DRISCOLL, J. F. 2008 Turbulent premixed combustion: flamelet structure and its effect on turbulent burning velocities. *Prog. Energy Combust. Sci.* **34**, 91–134.

DUPONT, T. F. & LIU, Y. J. 2007 Back and forth error compensation and correction methods for semi-Lagrangian schemes with application to level set interface computations. *Maths Comput.* **76**, 647–668.

EVANS, L. C. 1997 *Partial Differential Equations*. American Mathematical Society.

FRENKIEL, F. N. & KLEBANOFF, P. S. 1967 Higher-order correlations in a turbulent field. *Phys. Fluids* **10**, 507–520.

GROFF, E. G. 1987 An experimental evaluation of an entrainment flame-propagation model. *Combust. Flame* **67**, 153–162.

HEMCHANDRA, S. & LIEUWEN, T. 2010 Local consumption speed of turbulent premixed flames – an analysis of 'memory effects'. *Combust. Flame* **157**, 955–965.

HEMCHANDRA, S., PETERS, N. & LIEUWEN, T. 2011 Heat release response of acoustically forced turbulent premixed flames-role of kinematic restoration. *Proc. Combust. Inst.* **33**, 1609–1617.

HINZE, J. O. 1975 *Turbulence*. McGraw-Hill.

HUANG, Y., RATNER, A., YANG, V. & LU, T. 2009 Experimental investigation of thermoacoustic coupling for low-swirl lean premixed flames. *J. Propul. Power* **25**, 365–373.

HUANG, Y. & YANG, V. 2009 Dynamics and stability of lean-premixed swirl-stabilized combustion. *Prog. Energy Combust. Sci.* **35**, 293–364.

HUYGENS, C. 1962 *Treatise on Light*. Dover.

KARIMI, N., BREAR, M. J., JIN, S.-H. & MONTY, J. P. 2009 Linear and nonlinear forced response of a conical, ducted, laminar premixed flame. *Combust. Flame* **156**, 2201–2212.

KIM, K. T. & HOCHGREB, S. 2011 The nonlinear heat release response of stratified lean-premixed flames to acoustic velocity oscillations. *Combust. Flame* **158**, 2482–2499.

KURAMOTO, Y. & TSUZUKI, T. 1976 Persistent propagation of concentration waves in dissipative media far from thermal equilibrium. *Prog. Theor. Phys.* **55**, 356–369.

LAW, C. K. & SUNG, C. J. 2000 Structure, aerodynamics, and geometry of premixed flamelets. *Prog. Energy Combust. Sci.* **26**, 459–505.

LEE, D. H. & LIEUWEN, T. C. 2003 Premixed flame kinematics in a longitudinal acoustic field. *J. Propul. Power* **19**, 837–846.

LEE, J. G. & SANTAVICCA, D. A. 2003 Experimental diagnostics for the study of combustion instabilities in lean premixed combustors. *J. Propul. Power* **19**, 735–750.

LIEUWEN, T. 2003 Modeling premixed combustion-acoustic wave interactions: a review. *J. Propul. Power* **19**, 765–781.

LIEUWEN, T. C. & YANG, V. 2005 *Combustion Instabilities in Gas Turbine Engines: Operational Experience, Fundamental Mechanisms and Modeling*. AIAA.

LIPATNIKOV, A. N. & CHOMIAK, J. 2002 Turbulent flame speed and thickness: phenomenology, evaluation, and application in multi-dimensional simulations. *Prog. Energy Combust. Sci.* **28**, 1–74.

LIPATNIKOV, A. N. & CHOMIAK, J. 2004 Application of the Markstein number concept to curved turbulent flames. *Combust. Sci. Technol.* **176**, 331–358.

LIPATNIKOV, A. & CHOMIAK, J. 2007 Global stretch effects in premixed turbulent combustion. *Proc. Combust. Inst.* **31**, 1361–1368.

LIPATNIKOV, A. N. & SATHIAH, P. 2005 Effects of turbulent flame development on thermoacoustic oscillations. *Combust. Flame* **142**, 130–139.

MATALON, M. 1983 On flame stretch. *Combust. Sci. Technol.* **31**, 169–181.

MATALON, M. & MATKOWSKY, B. J. 1982 Flames as gas-dynamic discontinuities. *J. Fluid Mech.* **124**, 239–259.

MCMANUS, K. R., POINSOT, T. & CANDEL, S. M. 1993 A review of active control of combustion instabilities. *Prog. Energy Combust. Sci.* **19**, 1–29.

MOUREAU, V., FIORINA, B. & PITSCH, H. 2009 A level set formulation for premixed combustion LES considering the turbulent flame structure. *Combust. Flame* **156**, 801–812.

OSHER, S. & FEDKIW, R. P. 2003 *Level Set Methods and Dynamic Implicit Surfaces*. Springer.

PALIES, P., SCHULLER, T., DUROX, D. & CANDEL, S. 2011 Modeling of premixed swirling flames transfer functions. *Proc. Combust. Inst.* **33**, 2967–2974.

PENG, D. P., MERRIMAN, B., OSHER, S., ZHAO, H. K. & KANG, M. J. 1999 A PDE-based fast local level set method. *J. Comput. Phys.* **155**, 410–438.

PETER, S. 2006 The numerical approximation of a delta function with application to level set methods. *J. Comput. Phys.* **211**, 77–90.

PETERSEN, R. E. & EMMONS, H. W. 1961 Stability of laminar flames. *Phys. Fluids* **4**, 456–464.

POPE, S. B. 2000 *Turbulent Flows*. Cambridge University Press.

PRUDNIKOV, A. 1964 Combustion of homogeneous fuel-air mixtures in turbulent flows. In *Physical Basis of Processes in Combustion Chambers of Airbreathing Engines* (ed. B. V. Raushenbakh, S. A. Belyi, I. V. Bespalov, V. Y. Borodachev, M. S. Volynskii & A. G. Prudnikov). pp. 255–347. Mashinostroenie.

RASTIGEJEV, Y. & MATALON, M. 2006 Numerical simulation of flames as gas-dynamic discontinuities. *Combust. Theor. Model.* **10**, 459–481.

SEARBY, G. & ROCHWERGER, D. 1991 A parametric acoustic instability in premixed flames. *J. Fluid Mech.* **231**, 529–543.

SETHIAN, J. A. 1999 *Level Set Methods and Fast Marching Methods: Evolving Interfaces in Computational Geometry, Fluid Mechanics, Computer Vision, and Materials Science*. Cambridge University Press.

SHANBHOGUE, S. 2008 *Dynamics of Perturbed Exothermic Bluff-body Flow Fields*. Georgia Institute of Technology.

SHANBHOGUE, S., SHIN, D. H., HEMCHANDRA, S., PLAKS, D. & LIEUWEN, T. 2009*a* Flame sheet dynamics of bluff-body stabilized flames during longitudinal acoustic forcing. *Proc. Combust. Inst.* **32**, 1787–1794.

SHANBHOGUE, S. J., SEELHORST, M. & LIEUWEN, T. 2009*b* Vortex phase-jitter in acoustically excited bluff body flames. *Intl J. Spray Combust. Dyn.* **1**, 365–387.

SHIN, D. H. 2012 *Premixed Flame Kinematics in a Harmonically Oscillating Velocity Field*. Georgia Institute of Technology.

SHIN, D.-H. & LIEUWEN, T. 2012 Flame wrinkle destruction processes in harmonically forced, laminar premixed flames. *Combust. Flame* **159**, 3312–3322.

SHIN, D. H., PLAKS, D. V., LIEUWEN, T., MONDRAGON, U. M., BROWN, C. T. & MCDONELL, V. G. 2011 Dynamics of a longitudinally forced, bluff body stabilized flame. *J. Propul. Power* **27**, 105–116.

SIVASHINSKY, G. I. 1977 Nonlinear analysis of hydrodynamic instability in laminar flames – I. Derivation of basic equations. *Acta Astron.* **4**, 1177–1206.

THUMULURU, S. K. 2010 *Effect of Harmonic Forcing on Turbulent Flame Properties*. Georgia Institute of Technology.

TSUJI, H., GUPTA, A. K., HASEGAWA, T., KATSUKI, M., KISHIMOTO, K. & MORITA, M. 2002 *High Temperature Air Combustion: From Energy Conservation to Pollution Reduction*. CRC.

WANG, H. Y., LAW, C. K. & LIEUWEN, T. 2009 Linear response of stretch-affected premixed flames to flow oscillations. *Combust. Flame* **156**, 889–895.

WILLIAMS, F. A. 1985 *Combustion Theory*. Addison-Wesley.

ZIMONT, V. 1977 To computations of turbulent combustion of partially premixed gases. In *Chemical Physics of Combustion and Explosion Processes. Combustion of Multi-Phase and Gas Systems*, pp. 77–80 USSR Academy of Science.

ZIMONT, V. & LIPATNIKOV, A. 1995 A numerical model of premixed turbulent combustion of gases. *Chem. Phys. Rep.* **14**, 993–1025.